

Characterization of Perfluorooctylbromide-Based Nanoemulsion Particles Using Atomistic Molecular Dynamics Simulations

Sun-Joo Lee¹, Brett Olsen², Paul H. Schlesinger³, Nathan A. Baker⁴

June 21, 2010

¹Department of Biochemistry and Molecular Biophysics, Computational and Molecular Biophysics Graduate Program, Center for Computational Biology, Washington University in St. Louis

²Department of Biochemistry and Molecular Biophysics, Molecular Cell Biology Graduate Program, Center for Computational Biology, Washington University in St. Louis

³Department of Cell Biology and Physiology, Washington University in St. Louis, 660 South Euclid Avenue, Campus Box 8228, St. Louis, Missouri 63110

⁴To whom correspondence should be addressed. Department of Biochemistry and Molecular Biophysics, Center for Computational Biology, Washington University in St. Louis. 700 S. Euclid Ave., Campus Box 8036, St. Louis, MO 63110. Tel: 314-362-2040, E-mail: baker@ccb.wustl.edu, Web: <http://www.nabgroup.org>

Running title: Atomistic modeling of a PFOB-NEP interface

Keywords: Nanomedicine, Nanoemulsion particles, Perfluorooctylbromide, Phase separation, Atomistic molecular dynamics

Abstract

Perfluorocarbon-based nanoemulsion particles have arisen as promising platforms for the cellular delivery of imaging and therapeutic agents to specific targets. However, current knowledge of the agent delivery mechanism is limited to qualitative and phenomenological models. Lack of detail at the molecular level has hence delayed optimizing or customizing nanoemulsion particles for therapeutic and imaging applications. Here we report the first atomistic structural details of a perfluoroctylbromide-based (PFOB-based) nanoemulsion particle (NEP) with a 1-palmitoyl-2-oleoyl-phosphatidylcholine (POPC) lipid emulsifier. Newly developed PFOB force field parameters were used in molecular dynamics simulations to model the PFOB-NEP interface in a planar configuration. These PFOB force field parameters were developed and tested to reproduce the characteristics of bulk PFOB as well as PFOB at interfaces with water and emulsifying phospholipids. The modeled PFOB-NEP interface demonstrated significant intercalation of PFOB into the emulsifying lipid monolayer and consequent changes in the structural, electrostatic, and mechanical properties of the POPC monolayer and PFOB. This intercalation provides an explanation for experimental data demonstrating melittin tryptophan fluorescence quenching upon binding to the nanoemulsion particles through the observation of direct contact between the melittin tryptophan and the PFOB bromine. Additionally, the atomistic details of the PFOB-NEP interface structure provided by our simulations are used to suggest the influence of each component on PFOB-NEP delivery function which will be tested in future coarse-grained simulations.

1 Introduction

Nanoscale particles have been developed for wide range of applications in medicine (1). Medical applications include drug delivery (2), therapy (3, 4), *in vivo* imaging (5, 6), *in vitro* diagnostics (7), biomaterials research (8), and active implants (9). Among those applications, many studies have been focused on the development of nanoparticles as carriers of therapeutic and imaging agents. In nanomedicine, the delivery of therapeutic and imaging agents (cargo) is often accomplished by functionalized nanoscale particles (carriers) to which target-specific ligands are attached. Nanoparticle-based delivery using functionalized particles offers advantages over traditional small molecule therapies in that it can improve solubility, protect molecules from premature degradation and non-specific interactions, and increase the effective concentration of drugs in target tissues (10). Such advantages enhance the therapeutic efficacy while decreasing dosages and side effects (11).

One example of functionalized nanoparticles are nanoemulsion particles (NEPs): emulsion droplets with nanoscale dimensions. In particular, perfluorocarbon-based NEPs have been studied and developed for the delivery of therapeutic agents (12) and are the focus of the current study. We are particularly interested in a class of NEPs where the emulsion core is formed by hydrophobic perfluoroctylbromide (PFOB, C₈BrF₁₇) (see Figure 1B) and the core is enclosed by a phospholipid monolayer that functions as an emulsifier to stabilize the droplets (12, 13) (see Figure 1A). Perfluorocarbons (PFCs) are biologically inert, chemically stable, non-degradable, non-toxic, and non-volatile, which are all characteristics that make nanoemulsions biocompatible (12, 14–17). In particular, PFOB has been most commonly used due to its low vapor pressure that will reduce the likelihood of evaporation and the production of pulmonary emphysema (15, 18). In addition, the short half-life of PFOB in the body makes the molecule more practically applicable (16, 17). Finally, the emulsifying phospholipid monolayer is typically derived from either egg- or soybean-lecithin. Such phospholipid preparations have been used for many purposes in cosmetic, food, and drug applications (19).

There are already many biomedical applications of perfluorocarbon-based NEPs for imaging, diagnosis, and therapy. Perfluorocarbon-based NEPs have been used in magnetic resonance imaging (MRI) studies to detect and quantify fibrin protein, to define vessel geometry, and to track stem or progenitor cells(20–22). Fumagillin-loaded NEPs functionalized to target $\alpha_v\beta_3$ integrin significantly suppress neovasculature, thereby inhibiting tumor growth (11). Recently PFOB-NEP has been developed as a platform to deliver melittin, a cytolytic peptide, to cancer cells, illustrating the potential of using cytolytic peptides for chemotherapy (13, 23).

Macroscopic experimental observations suggest a two-step mechanism for delivery of cargo molecules from perfluorocarbon-based NEPs to the cytoplasm of the target cells (24). First, cargo molecules are delivered from NEPs to target plasma membranes via passive diffusion, so called “contact-facilitated” delivery that takes place after the NEPs bind to or closely approach the target cell surface (25). Next, the cargo molecules are transported from the plasma membrane into the cytoplasm by active raft-dependent internalization at the cost of ATP hydrolysis (24). However, the molecular details of both steps are largely unknown and must be understood in order to rationally design particles which achieve optimal delivery

efficiency.

Our long term goal is to describe and understand the molecular details of cargo delivery from PFOB-NEP to target membranes via this contact-facilitated mechanism. A lipid complex, resembling the hemifusion stalk intermediate from bilayer fusion, was hypothesized to form between the PFOB-NEP phospholipid monolayer and the outer monolayer of the target cell plasma membrane. Considering the relatively small dimensions of hemifusion stalks (26), we plan to use computational simulations at both atomistic and coarse-grained levels to examine the structural details of this intermediate as well as the functional roles of the component molecules.

As a first step towards this long-term goal, we parameterized the PFOB core at an atomistic level. We simulated a model PFOB-NEP interface in a planar configuration using our new PFOB parameters. The accuracy of our parameters was tested against several experimental measurements while the accuracy of our PFOB-NEP interface was examined using melittin as a molecular ruler in the following manner. Efficient tryptophan (Trp) fluorescence quenching by bromine atoms can occur only when the two molecules appose very closely (27), and we observe this quenching when melittin binds to the surface of PFOB-NEPs (13). In our simulations, PFOB bromine was observed to approach the melittin Trp side chain closely enough to quench Trp fluorescence. This observation provides a viable mechanism for the melittin Trp quenching by resolving a contradiction in assumptions about PFOB-NEP structure (28). Furthermore, the model provides insight into the roles of the molecular components on PFOB-NEP structure and function, thus offering a basis for future engineering and design of PFOB-NEPs.

2 Methods

2.1 Parameterization

Force field parameters for perfluorocarbons (CF_2 and CF_3) were developed at the united atom level of resolution for consistency with the Berger et al. lipid force fields (29) commonly used in biomembrane simulations (30–33). United atom force field parameters for perfluorocarbons were previously developed by Shin et al., using σ values for the Lennard-Jones (LJ) interaction obtained from lattice spacing of solid perfluoroalkanes and ϵ values derived by modulating the ϵ of $\text{CH}_2\text{-CH}_2$ and $\text{CH}_3\text{-CH}_3$ based on the polarizability of the bond (34). Hariharan and Harris modified the parameters introduced by Shin et al. by decreasing σ and slightly increasing ϵ values (35). Hariharan and Harris reported that the modified parameters reproduced the experimental density within 2% error; however, the surface tension was much larger than the experimentally measured, indicating the parameters still needed improvement (35). Cui et al. independently developed perfluorocarbon parameter sets that had very similar σ values to the Harihan model but a smaller ϵ for CF_2 and a greater ϵ for CF_3 . The Cui et al. parameters reproduced experimental density and vapor-liquid equilibria (36); however, these could only reproduce liquid phase densities with 95% accuracy. None of the pre-existing force field parameters modeled pure perfluorocarbons with the accuracy desired for our study; therefore, they were not tested to see if they properly modeled the interface between perfluorinated molecules, emulsifying lipids, and water. In our study, the

emulsifying interface between PFOB and water is the most important region because of its role in NEP functions including cargo binding and delivery. Therefore, in this study, new parameter sets were generated with a particular emphasis on PFOB interfacial behavior, while maintaining or improving the thermodynamic behavior described by past force fields.

PFOB molecules were modeled with an explicit bromine atom and two united atom types: PC (intermediate CF_2) and PEC (terminal CF_3). Bond and angle terms were taken from the OPLS-AA force field (37). Torsional parameters were derived from the rotational energy profiles of two model compounds: $\text{Br}-\text{CF}_2-\text{CF}_2-\text{CF}_3$ and $\text{CF}_3-\text{CF}_2-\text{CF}_2-\text{CF}_3$. Single point energies were calculated after structural optimization with torsional angles fixed at 15° increments, using *ab initio* calculations with the B3LYP functional in combination with the $cc-p$ VTZ-PP basis set (38). The coefficients of the Ryckaert-Bellemans (RB) dihedral potential function (39) were fit to the potential profiles by a linear least squares method (see Figure 1 of the Supporting Information).

Electrostatic potential (ESP) charges (40) were determined for an optimized PFOB molecule in vacuum by *ab initio* calculations with the B3LYP functional in combination with the $cc-p$ VTZ-PP basis set. Charges for the united atoms were obtained by summing the partial charges of the atoms comprising each united atom. The LJ parameters for PC and PEC united atoms were taken and optimized from the previous work (34); in particular, the size parameters (σ) were systematically varied to reproduce the density and heat of vaporization of liquid PFOB. The resulting force field parameters are summarized in Table 1, while tests of these parameters are summarized in the Table 2, the details of the tests are described in Supporting Information. We observed much better accuracy in united-atom perfluoromethane solvation energies in united atom *n*-hexane models rather than an all-atom perfluoromethane model. The united atom *n*-hexane models closely resemble the tail region of the lipid models used in our simulations. Therefore, these results support the compatibility of our model with the current lipid models.

2.2 Simulations

2.2.1 Initial structures

Planar PFOB-based nanoemulsion interface model A PFOB-based nanoemulsion particle (PFOB-NEP) interface was modeled in a planar configuration (see Figure 2). A similar “sandwich” topology was previously used by other researchers to simulate an emulsion composed of a triglyceride core and a phospholipid monolayer in water (41). The interface model was constructed from structures of POPC monolayers composed of 64 1-palmitoyl-2-oleoyl phosphatidylcholine (POPC) lipids extracted from a previous POPC bilayer simulation (33). These two POPC monolayers were then placed in a periodic box in an arrangement that separated lipid tails by 15.3 nm and the headgroups by 6 nm. The space flanked by tails (inside) was filled with 1310 PFOB molecules while the other space facing the head groups (outside) was filled with 11,678 water molecules. The system was fully hydrated with 91.2 waters per lipid (42). This system will be referred to as PFOB-NEP throughout this report.

Melittin peptides bound to the planar PFOB-NEP interface The initial configuration of melittin bound to the planar PFOB-NEP interface was based on experimental results.

First, it was shown experimentally that melittin did not disrupt the monolayer of PFOB-NEP even at high mole fraction of melittin (lipid/melittin molar ratio, 40) (13). Second, melittin was found to sit on the water-lipid interface of bilayer surface at low concentration without exerting cytolytic activity (43). These experimental data suggested that melittin is likely to reside at the water-lipid interface of the monolayer and, accordingly, the initial structure was constructed as described below.

The initial structure was prepared with an equilibrated PFOB-NEP interface structure obtained from the simulations described above and a model of bilayer-bound melittin provided by the Hristova and White groups (43). A single melittin peptide was inserted into each POPC monolayer to the depth of the glycerol groups (see Figure 11) as suggested by experimental results (43). The peptide was inserted so that its non-polar residues faced the hydrophobic interior while its polar residues faced the NEP-water interface. POPC lipids that significantly overlapped with the inserted melittin peptides were deleted, leaving 55 POPC lipids remaining in each monolayer. No PFOB molecules had direct contact with the inserted melittin peptides and hence none of them were deleted. 19,958 water molecules were added to solvate the system. To neutralize the +5 formal charge of each melittin peptide, ten randomly chosen water molecules were replaced by chloride ions. The hydration level of the system was approximately 90 water molecules per lipid.

2.2.2 Force field parameters

POPC was modeled with the united atom force field parameters optimized by Berger et al. (29) and Chiu et al. (44). Water was modeled by the simple point charge SPC model (45).

Generally, mixing of two different force fields is not recommended and sometimes not feasible due to different functional forms and combination rules. However, Tieleman et al. (31) have reported that OPLS-AA (46) all-atom protein representations could be successfully used in combination with the united-atom lipid model described above. In our system, such a combination of parameters prevents artificial condensation of the membrane by eliminating overly-favorable lipid-protein interactions, otherwise use of standard GROMOS united atom types may cause significant condensation of the membrane (31). Therefore, the melittin peptides used in these simulations were modeled with the OPLS-AA force field (46). The combination of these two different force fields for lipids and peptides was made possible by using a half-epsilon and double pair list method (47) to resolve the different 1-4 interaction scaling factors used by the two force fields (48). Our simulation used OPLS-AA combination rules; however, the parameters for van der Waals (vdW) interaction energy for the 1-4 interaction pairs were listed by their half magnitude in the parameter file for non-bonded interactions. The 1-4 interaction pair list was repeated twice in the lipid topology file. By doing so, the 1-4 interaction energy of lipid that originally use GROMACS combination rule could be scaled properly while the combination rule of OPLS-AA force field was used. This method was tested using both a pure POPC bilayer and bulk PFOB, and both the bilayer area and the bulk PFOB density were identical within error to identical simulations using standard combination rules (data not shown).

2.2.3 Simulation parameters

Molecular dynamics simulations and analyses of the trajectory were performed with GROMACS version 4.0 (48). The starting structures were subjected to previously described equilibration procedures (49). First, an energy minimization was performed using a steepest descent method and the system was then gradually heated from 50 K to 303 K through a series of short molecular dynamics (MD) simulations. After the system reached the production temperature of 303 K, the MD simulation was continued for at least 150 ns of production simulation. The cutoffs for LJ interaction and for direct space for electrostatic interactions were 1.0 nm. The particle-mesh Ewald method (50) with conducting boundary conditions was used for long-range electrostatic interactions. The simulation was performed in an isobaric-isothermal ensemble (NpT). A Parrinello-Rahman barostat (51) with 2 ps coupling time was used to maintain the system pressure at 1 bar. The pressure coupling type varied depending on the systems: isotropic pressure coupling was used for simulations of bulk solutions, semiisotropic for simulations of PFOB-NEP interface and POPC bilayer systems, and anisotropic for the simulation of melittin bound membranes. A Nosé-Hoover thermostat (52) with 0.5 ps coupling frequency was applied to each molecule type separately. Hydrogen atoms bonded to heavy atoms were constrained with the LINCS algorithm (53), allowing a 2 fs time step to be used.

2.3 Analysis

2.3.1 Block averaging

To perform statistical analysis, each trajectory was divided into small blocks with the block size chosen based on the standard error so that each block was independent of one another (54). The standard error $\varepsilon(f, n)$ in observable f for a block of length n was calculated according to the formula $\varepsilon(f, n) = \sigma / \sqrt{M}$, where n is the block length, σ is mean standard deviation, and M is the number of blocks in the simulation. When the block size is large enough; e.g., much greater than the correlation time of an observable, the standard errors become independent of the block size and the true standard error is obtained. The block size for sub-sampling was determined by the value of n where $\varepsilon(f, n)$ for observable f reached a plateau.

3 Results

3.1 Characterization of the PFOB-NEP interface

3.1.1 Equilibration and sub-sampling

Two independent simulations of the PFOB-NEP interface shown in Figure 2 were performed for 150 ns; a control POPC bilayer was simulated for 300 ns. After equilibration, the PFOB in the PFOB-NEP “sandwich” became denser than in the more loosely distributed initial state. This change was accompanied by the intercalation of PFOB into the monolayer as

shown in the right panel of Figure 2 and in the number density profile of the molecules along the z-axis (Figure 3).

The cross-sectional area of total membranes was used to determine the equilibration of the system. The three simulated systems showed no significant area drifts throughout the simulations, implying that the systems quickly reached equilibrium during the temperature equilibration steps (see Figure 5 of Supporting Information). To further ensure unbiased results, the first 10 ns of each trajectory was discarded for analysis to remove any possible bias from the starting structure.

The fluctuation of the cross-sectional area of total membrane was also used to determine the statistically-independent block size for each trajectory to calculate standard error as explained in the section 2.3.1. For the two PFOB-NEP interface simulations, the standard error reached a plateau with a 14 ns block size and, beyond that size, the increase in standard errors was marginal. Therefore, 10 independent blocks of 14 ns each were generated from each trajectory and results from each block were combined to compute means and standard errors.

The same test was performed for the control POPC bilayer, and with 14 ns block size, the standard error stopped increasing drastically and only small increases were observed for much larger block sizes. With a 14 ns block size, 20 statistically independent blocks were obtained from the control POPC bilayer simulation. The observables calculated in this report were averaged over the statistically independent blocks as determined in this section.

3.1.2 NEP-water interface geometry

Figure 4 shows that the width δ of PFOB and SPC water at the emulsion interface increases substantially as compared with the pure PFOB-water interface shown in Figure 3 of the Supporting Information. Additionally, the PFOB and water density profiles overlap only slightly in the presence of the POPC monolayer demonstrating the effectiveness of the stabilizing monolayer at separating the hydrophobic PFOB molecules from the aqueous environment.

Monolayer density distribution The number density profiles of the monolayer along the z-axis were determined to assess structural changes in the POPC monolayers. Two density profiles of the PFOB-NEP interface and the control POPC bilayer were aligned such that the maximum density of each was placed at zero on the z-axis. Figure 5 shows that the thickness of the monolayer is greater in the PFOB-NEP interface than in individual control bilayer leaflets. The largest increase in thickness was observed in the tail region of the PFOB-NEP interface monolayer. The maxima of the density profiles of different parts of lipids shifted outwards as compared to those of the control POPC bilayer. The peak of choline group shifted toward the water side and terminal methyl group shifted toward the lipid tail side. These density shifts are consistent with the more parallel orientation of the P-N vector to the bilayer normal (see Figure 8) and more ordered lipid tails (see Figure 7).

Total area The cross-sectional area of a lipid molecule has been a commonly used metric to assess and compare membranes under different physical environments or with different force field parameters (33, 55, 56) However, as described previously (33), it is not a trivial problem

to measure the cross-sectional area of individual lipids in inhomogeneous membranes. As described above, the POPC monolayers of PFOB-NEP interface were inhomogeneous due to the intercalation of PFOB. Therefore, the cross-sectional area of the total monolayer, which corresponds to the lateral area (XY-plane) of the simulation box, was measured and compared with that of the control POPC bilayer instead. The cross-sectional area of 128 POPC bilayer ($41.0 \pm 0.1 \text{ nm}^2$) gives a per-lipid area of $0.641 \pm 0.001 \text{ nm}^2$ which is in good agreement with both experiment (55) and with the results of other simulations (56). The expansion of the cross-sectional total membrane area of PFOB-NEP interface compared to the control POPC bilayer is shown in Figure 6A. The mean areas and standard errors obtained from the independent blocks were 44.42 ± 0.17 for the 64-lipid PFOB-NEP interface and the increase was significant (99.9% confidence level). The result agrees qualitatively with experimental Langmuir results that show total monolayer area expansion upon the application of gaseous PFOB to the hydrophobic tail side of the monolayer (57).

Probe-accessible surface area Probe-accessible surface area (ASA) was measured using a 1.4 \AA probe to examine the contribution of each molecule to the area expansion. The contributions of hydrophilic and hydrophobic parts of the system to the total ASA were calculated separately. The hydrophilic parts consisted of all POPC headgroup atoms, while the hydrophobic parts consisted of lipid tails and PFOB.

In agreement with the total membrane area results, the total ASA of the PFOB-NEP interface was greater than that of control POPC bilayer. The increase in the total ASA could be fully attributed to the increased hydrophilic ASA; hydrophobic ASA decreased in the PFOB-NEP interface. The lower inset of Figure 6B shows the contribution of POPC lipid tails and PFOB to the hydrophobic ASA. The surface exposure of lipid tails was substantially decreased while a small portion of the hydrophobic surface area was contributed by PFOB molecules at the PFOB-NEP interface. The reduction in hydrophobic ASA could be explained by the intercalation of PFOB in between the lipid tails. The void volume in between lipid tails in POPC bilayer provides continuous paths through which water probe could travel into the hydrophobic interior of POPC bilayer; however, those paths were blocked by intercalated PFOB molecules in the PFOB-NEP interface which resulted in a substantially decreased hydrophobic surface area.

Order parameters Lipid tail order parameters provide important details about membrane structure (33, 58). Figure 7 clearly shows that tail order parameters for POFB-NEP interface lipids increased, with respect to POPC bilayers, for both chains all along the tail length. This increase was most prominent near the ends of the lipid tails. In the control bilayer, the ends of lipid tails are more flexible and have smaller order parameters due to the void volume at the center of bilayers. In the PFOB-NEP interface, no void volume exists at the hydrophobic region and, hence, conformational flexibility decreases more substantially near the termini of lipid tails. Increased order parameters indicates that POPC molecules are in more extended conformations and occupy a smaller cross-sectional area per lipid. This result clearly supports our conclusion that the expanded total monolayer area is due to the intercalation of PFOB molecules into the POPC monolayers and not due to the disordering of POPC.

Head group orientation The P-N vector (see Figure 1B) connects the POPC phosphorus and nitrogen atoms and reorients in response to environmental changes. The orientation was computed to obtain $\cos \theta$ where θ is the angle between the mean P-N vector and the monolayer normal. Larger values of $\cos \theta$ indicate a P-N vector orientation that is more parallel with respect to the monolayer normal. Figure 8 shows significantly greater $\cos \theta$ value in the PFOB-NEP interface as compared to POPC bilayers. Decreased electrostatic repulsion among the head group dipoles due to expanded monolayer area likely caused this more parallel distribution of P-N vectors. While this change in orientation was significant, no increased net polarization density was measured (see Figure 6 in the Supporting Information), indicating compensatory polarization changes in the rest of the system.

3.1.3 Characterization of PFOB structure

Shape Conformational variation of PFOB along the z-axis was examined. The short chain length of PFOB resulted in no significant variation of the radius of gyration along the z-axis (data not shown). Therefore, the average conformation of PFOB along the z-axis was examined by assessing the mean end-to-end length from Br to CF_3 (see Figure 9B). The mean end-to-end length was 1.02 nm in a fully extended conformation and 0.992 ± 0.002 nm for bulk PFOB. To obtain a profile of PFOB in the emulsion environment, the simulation system was divided into slabs of 0.25 nm thickness along the z-axis, and then mean length was computed from the average over the molecules in an individual slab. Figure 9A shows that the PFOB conformation has small but significant variations along the z-axis. The PFOB length was longer within the monolayers, indicating that more PFOBs were in extended conformations inside of the monolayers. On the other hand, the mean length was shortest near the lipid termini where the mixing of lipid tails and PFOB occurs. The mean end-to-end length at the middle of the PFOB-NEP interface was comparable to the mean length of bulk PFOB, indicating that the direct influence of the emulsifying monolayers vanished in the middle of the PFOB-NEP interface.

Orientation The mean orientation of PFOB along the z-axis was also examined. The molecular vector of PFOB is defined in Figure 1B starting from Br and pointing to the terminal CF_3 atom. The orientation was measured from the normalized inner product of the PFOB molecular vector with a unit vector along the z-axis. The orientation of every PFOB was averaged over slabs of 0.25 nm thickness along the z-axis and plotted in Figure 9B.

The plot shows that PFOB inside and adjacent to the monolayers was preferentially oriented. The maximum peaks with the $\cos \theta = 0.3$ appeared inside of the monolayers, showing that PFOB preferentially orients with its Br atom pointing to the hydrophilic surface of the monolayer. The preferential orientations vanished very quickly outside of the monolayers, and PFOB was randomly oriented with the $\cos \theta$ zero in the middle of the PFOB-NEP interface, which again supports the assertion that the PFOB-NEP sandwich geometry can be appropriately used to model larger nanoemulsion droplet interfaces.

The preferentially oriented PFOB in the monolayers contributed additional non-zero charge density to the system as shown in Figure 9C. The charge attributed to the preferentially oriented PFOB generated additional positive electrostatic potential inside of the

PFOB-NEP interface, which will be discussed in the section 3.1.4.

3.1.4 Electrostatic potential profile

The charge density profiles of the pure POPC bilayer (top) and the PFOB-NEP interface (middle and bottom) are shown in Figure 10A. The overall charge density profiles of the pure POPC bilayer and that of the PFOB-NEP monolayer are almost indistinguishable. The PFOB charge densities of the PFOB-NEP interface are plotted separately due to their much smaller scale compared to those of POPC and water. The sinusoidal fluctuation of PFOB charge in and near the POPC monolayer was observed and attributed to the polarized molecular orientation of PFOB molecules discussed earlier in the previous section (3.1.3).

The electrostatic potential was calculated by the double integration of the charge densities along the z-axis as shown in the following equation (59, 60).

$$\phi(z) - \phi(0) = -\frac{1}{\epsilon} \int_0^z \left(\int_0^{z'} \rho(z'') dz'' + D_0 \right) dz', \quad (1)$$

where ϵ is a *homogeneous* dielectric constant which is ϵ_0 for analysis of the atomistic system, and $\rho(z)$ is the charge density. The displacement constant D_0 for net neutral systems to impose the conducting boundary condition is defined by (59, 60)

$$D_0 = -\frac{1}{L} \int_0^L \int_0^z \rho(z'') dz'' dz, \quad (2)$$

Results are shown in Figure 10B. The statistical errors in the electrostatic potential along the z-axis were small and are not shown for clarity. The black curves in the figure showed that electrostatic potentials of the PFOB-NEP interface and POPC bilayer systems were substantially different. The positive potential in the interior of PFOB-NEP was much greater than the potential at the hydrophobic interior of pure POPC bilayer. The potentials due to different molecules were estimated separately to identify the origin of this positive potential (see Figure 7 of the Supporting Information). It was observed that the potentials due to both POPC and water of the PFOB-NEP interface system were comparable to the potentials of pure POPC bilayer system. The additional positive potential was attributed solely to the dipolar charge distribution of PFOB due to their polarized orientation near the PFOB-NEP monolayer.

Another minor difference between the two systems is the slightly lower potential at the boundary peak. The decreased potential can be explained by the greater total membrane area and concomitantly decreased charge density in the PFOB-NEP interface system.

3.2 Testing the model with melittin tryptophan fluorescence quenching

Melittin was simulated to test if the modeled system agrees with experimental results in that Trp fluorescence was quenched upon melittin binding on the surface of PFOB-NEP (13) and to elucidate the molecular mechanism of the quenching phenomenon. The quenching of Trp

fluorescence by bromine atom is known to occur within very short distances via dynamics quenching mechanism (27, 61). Therefore, in order for quenching to occur, bromine atoms must directly collide with Trp side chain.

A simulation with melittin at the NEP interface was performed for 190 ns as described in the Methods sections 2.2.2 and 2.2.3. The initial structure and position of melittin was based on x-ray diffraction results which show that, at low mole fractions, melittin positions itself parallel to the membrane surface at the depth of the glycerol groups and orients its hydrophobic residues towards the hydrophobic interior of the membrane (43). Figure 11A shows the structure of the system after 190 ns of simulation. Figure 11B shows that melittin maintains a helical conformation, in agreement with experiments, (43) and that the Trp side chain faces the interior of the PFOB-NEP interface.

The radial distribution of bromine atoms around each Trp side chain was computed to assess the likelihood of quenching, and the radial distribution profiles of both peptides are shown in Figure 11C. The density of bromine atoms appeared at distance shorter or near the direct contact between the Trp side chain and bromine atoms considering the radii of the two (approximately 0.35 nm and 0.33 nm respectively) (61). Such close apposition is made possible only through the intercalation of PFOB molecules into the monolayers and provides a molecular explanation of Trp quenching upon melittin binding to PFOB-NEP interfaces. This result, in turn, supports our modeled PFOB-NEP interface structure characterized by the PFOB intercalation.

4 Discussion

In this study, a new set of force field parameters for PFOB was developed to study the structural properties of a PFOB-NEP interface. The atomistic simulations show that PFOB intercalates into the emulsifying monolayers and causes unique structural changes at the NEP-water interfaces. Due to the intercalation, the structures and properties of the monolayer are altered, becoming distinct from those of similarly composed bilayers. Also, the orientation and conformation of PFOB was different within and near the monolayers as compared with bulk PFOB or the center of the PFOB-NEP interface. Such changes likely contribute to the functions of PFOB-NEP interface of cargo loading as well as cargo delivery.

4.1 United atom model for PFOB

The new set of force field parameters preserved important characteristics of PFOB both in bulk and at the phase-separated interface between water and PFOB both in the absence and presence of emulsifying phospholipid monolayer. The bulk density and heat of vaporization were reproduced in an acceptable accuracy. The strong hydrophobicity of the model PFOB generates a sharp interface in water and the computed surface tension from the interfaces was close to the experimentally measured value. While perfluorocarbon is regarded as lipophobic (28), the unfavorable solvation free energy of a perfluoromethane in liquid *n*-hexane (2.06 kJ/mol) (62) was less than thermal energy (2.48 kJ/mol) at room temperature. The strong hydrophobicity with relatively moderate lipophobicity of perfluorocarbon is important to form stable emulsions. Our parameters preserved the weakly unfavorable interaction between

perfluorocarbon united atom and the united *n*-hexane and, as a result, substantial mixing between PFOB and lipid tails is observed in our simulation.

4.2 System configuration caveats

The interface between PFOB and water was planar and was not allowed to have any large scale curvature due to the periodic boundary conditions and small lateral dimensions in our simulations. However, this planar interface can be considered to be equivalent to small patches on the surface of larger PFOB-NEPs with radii of a few hundred nanometers. Furthermore, because we observe a return to bulk PFOB behavior in the center of our sandwich simulation geometries, they can therefore be considered to mimic the interface of more realistic PFOB-NEPs. A similar simplification scheme has been used to model triglyceride-based emulsions (41) and to mimic cells that have asymmetric ionic conditions inside and outside of the cell by putting two bilayers in a simulation box (32, 49, 60).

In the current study, structural differences in the emulsifying monolayer of the PFOB-NEP have been assessed through comparison with a lipid bilayer of the same lipid composition. As a control, a bilayer is less topologically relevant than the monolayer at the air/water interface, which has been modeled recently (63, 64). However, a bilayer has been used as a control in our study to have a consistent comparison with future simulations designed to understand the functional mechanism of cargo delivery by using PFOB-NEPs as platforms. In particular, we wish to understand the differential binding of cargo, such as melittin peptides, to monolayers of PFOB-NEPs and the target bilayer membranes. Therefore, comparisons with a bilayer will provide us not only consistency with the future work but also more insight to understand the functional mechanisms of PFOB-NEPs.

4.3 PFOB intercalation into phospholipid monolayer

Substantial intercalation of PFOB into POPC monolayers was the most striking result of these simulations, and is somewhat contradictory to the expectation that PFOB and lipid tail would have a clear interface due to the lipophobicity of perfluorocarbons (28). However, models based on this expectation cannot explain the Trp fluorescence quenching that requires direct contact between the side chain and bromine atoms. Gerber et al examined the influence of gaseous perfluorocarbons (gFCs) on Langmuir DPPC monolayers and showed that gFCs had a strong fluidizing effect on the monolayer, expanded the total area, with more pronounced effects if the gFCs were linear (57). The results indicated that gFC interacts with the lipid tails. The fact that linear gFCs are more effective at causing such changes strongly suggests that the effect is mediated by the intercalation of gFCs with the lipid tails. Yokoyama et al tested the miscibility of perfluorocarbons of various lengths (FC_n) and showed that the length of FC_n with respect to the lipid tail length is important in determining their miscibility: FC_n shorter than the lipid tail is miscible with lipid tails, miscibility drops as the FC_n length becomes closer to the tail length, and FC_n becomes immiscible if the length is comparable or greater than the tail length (65). These observations support our modeled PFOB-NEP interface since the PFOB chain length (FC_8) is far shorter than either the palmitoyl (C16) or oleoyl (C18) lipid tails of POPC. Finally, our simulation of melittin

peptide loaded onto PFOB-NEP interface corroborates the presence of this intercalation, in that PFOB intercalation is necessary for the tryptophan fluorescence quenching to occur by direct collision with bromine atoms (61).

5 Conclusions

Despite active research to develop PFOB-NEPs as platforms for carrying therapeutic agents, their atomistic structural details are yet to be determined, and limited knowledge hinders the rational design of the NEPs for optimal efficiency. This study is the first to report the structural details of the PFOB-NEP interface at an atomistic level. The reported interface structure is corroborated by providing a structural explanation for Trp quenching upon the melittin binding on the PFOB-NEP interface. More importantly this work opens new possibilities to study; in particular, the influence of different lipid compositions on the structure of the PFOB-NEP interface as well as cargo binding to the interface. Finally, the atomistic structural details of PFOB-NEP interface in the absence (pure PFOB-NEP interface) or presence of cargo (melittin peptides in this report) can be used as reference structures to develop coarse-grained models of the PFOB-NEP system. Simulation of the systems at a coarse-grained level will enable us to study behaviors on a much larger scale, such as the hypothesized lipid complex formation as well as cargo diffusion through the complex, which are under extensive study in our group.

Acknowledgments

The authors would like to thank Dr. Samuel Wickline and Dr. Greg Lanza for collaborations and helpful discussions, as well as Stephen H. White and Kalina Hristova for providing melittin-membrane models for our simulations. Computational resources were provided by the Texas Advanced Computing Center through Teragrid Grants TG-MCB060053 and TG-MCA08X003 as well as the National Biomedical Computation Resource (NIH P41 RR0860516). The current study was performed as part of the Siteman Center for Cancer Nanotechnology Excellence, supported by NIH grant U54 CA11934205.

5.1 Supporting Information

The supporting information includes 1) united atom PFOB model development, 2) United atom PFOB model testing (density, heat of vaporization, solvation free energy, and surface tension), and 3) PFOB-NEP analysis (total cross sectional area evolution, PFOB-NEP lipid head group polarization, and electrostatic potential due to individual components of the PFOB-NEP system). This information is available free of charge via the Internet at <http://pubs.acs.org>.

References

- [1] Volker Wagner, Anwyn Dullaart, Anne-Katrin Bock, and Axel Zweck. *Nat. Biotechnol.*, **24**(10), 1211–1217, 2006.
- [2] Kumares S. Soppimath, Tejraj M. Aminabhavi, Anand Rao R. Kulkarni, and Walter E. Rudzinski. *J. Control. Release*, **70**(1-2), 1–20, 2001.
- [3] I. Chen Wang, Lin A. Tai, Don D. Lee, P. P. Kanakamma, Clifton K. F. Shen, Tien-Yau Luh, Chien H. Cheng, and Kuo C. Hwang. *J. Med. Chem.*, **42**(22), 4614–4620, 1999.
- [4] Pallab Pradhan, Jyotsnendu Giri, Gopal Samanta, Haladhar D. Sarma, Kaushala P. Mishra, Jayesh Bellare, Rinti Banerjee, and Dhirendra Bahadur. *J. Biomed. Mater. Res. B*, **81B**(1), 12–22, 2007.
- [5] Patrick M. Winter, Shelton D. Caruthers, Andrea Kassner, Thomas D. Harris, Lori K. Chinen, John S. Allen, Elizabeth K. Lacy, Huiying Zhang, J. David Robertson, Samuel A. Wickline, and Gregory M. Lanza. *Cancer Res.*, **63**(18), 5838–5843, 2003.
- [6] Patrick M. Winter, Anne M. Morawski, Shelton D. Caruthers, Ralph W. Fuhrhop, Huiying Zhang, Todd A. Williams, John S. Allen, Elizabeth K. Lacy, J. David Robertson, Gregory M. Lanza, and Samuel A. Wickline. *Circulation*, **108**(18), 2270–2274, 2003.
- [7] Samira Bührer-Sékula, Henk L. Smits, George C. Gussenoven, J. van Leeuwen, S. Amador, Tsuyoshi T. Fujiwara, Paul R. Klatser, and Linda Oskam. *J. Clin. Microbiol.*, **41**(5), 1991–1995, 2003.
- [8] Kyung M. Woo, Ji-Hae Jun, Victor J. Chen, Jihye Seo, Jeong-Hwa Baek, Hyun-mo Ryoo, Gwan-Shik Kim, Martha J. Somerman, and Peter X. Ma. *Biomaterials*, **28**(2), 335–343, 2007.
- [9] James D. Weiland, Wentai Liu, and Mark S. Humayun. *Annu. Rev. Biomed. Eng.*, **7**(1), 361–401, 2005.
- [10] Shelton D. Caruthers, Samuel A. Wickline, and Gregory M. Lanza. *Curr. Opin. Biotech.*, **18**(1), 26–30, 2007.
- [11] Patrick M. Winter, Anne M. Neubauer, Shelton D. Caruthers, Thomas D. Harris, J. David Robertson, Todd A. Williams, Anne H. Schmieder, Grace Hu, John S. Allen, Elizabeth K. Lacy, Huiying Zhang, Samuel A. Wickline, and Gregory M. Lanza. *Arterioscler. Thromb. Vasc. Biol.*, **26**(9), 2103–2109, 2006.
- [12] Megan Kaneda, Shelton Caruthers, Gregory Lanza, and Samuel Wickline. *Ann. Biomed. Eng.*, **37**(10), 1922–1933, 2009.
- [13] Neelesh R. Soman, Gregory M. Lanza, John M. Heuser, Paul H. Schlesinger, and Samuel A. Wickline. *Nano Lett.*, **8**(4), 1131–1136, 2008.

- [14] Robert F. Mattrey, F. William Scheible, Barbara B. Gosink, George R. Leopold, David M. Long, and Charles B. Higgins. *Radiology*, **145**(3), 759–762, 1982.
- [15] Robert F. Mattrey. *Am. J. Roentgenol.*, **152**(2), 247–252, 1989.
- [16] Robert F. Mattrey and David M. Long. *Invest. Radiol.*, **23** (Suppl. 1), S298–S301, 1988.
- [17] Michael André, Thomas Nelson, and Robert Mattrey. *Invest. Radiol.*, **25**(9), 983–987, 1990.
- [18] Jeffry G. Weers. *J. Fluorine Chem.*, **64**(1-2), 73–93, 1993.
- [19] Margherita Rossi. Use of lecithin and lecithin fractions. In R. Huopalahti, R. Lopez-Fandino, M. Anton, and R. Schade, editors, *Bioactive Egg Compounds*, chapter 27, pages 229–239. Springer Berlin Heidelberg, 2007.
- [20] Anne M. Morawski, Patrick M. Winter, Xin Yu, Ralph W. Fuhrhop, Michael J. Scott, Franklin Hockett, David D. Robertson, Patrick J. Gaffney, Gregory M. Lanza, and Samuel A. Wickline. *Magnet. Reson. Med.*, **52**(6), 1255–1262, 2004.
- [21] Anne M. Neubauer, Shelton D. Caruthers, Franklin D. Hockett, Tillman Cyrus, J. David Robertson, J. Stacy Allen, Todd D. Williams, Ralph W. Fuhrhop, Gregory M. Lanza, and Samuel A. Wickline. *J. Cardiovasc. Magn. Reson.*, **9**(3), 565–573, 2007.
- [22] Kathryn C. Partlow, Junjie Chen, Jason A. Brant, Anne M. Neubauer, Todd E. Meyeroose, Michael H. Creer, Jan A. Nolta, Shelton D. Caruthers, Gregory M. Lanza, and Samuel A. Wickline. *FASEB J.*, **21**(8), 1647–1654, 2007.
- [23] Neelesh R. Soman, Steven L. Baldwin, Grace Hu, Jon N. Marsh, Gregory M. Lanza, John E. Heuser, Jeffrey M. Arbeit, Samuel A. Wickline, and Paul H. Schlesinger. *J. Clin. Invest.*, **119**(9), 2830–2842, 2009.
- [24] Kathryn C. Partlow, Gregory M. Lanza, and Samuel A. Wickline. *Biomaterials*, **29**(23), 3367–3375, 2008.
- [25] Gregory M. Lanza, Xin Yu, Patrick M. Winter, Dana R. Abendschein, Kerry K. Karukstis, Michael J. Scott, Lori K. Chinen, Ralph W. Fuhrhop, David E. Scherrer, and Samuel A. Wickline. *Circulation*, **106**(22), 2842–2847, 2002.
- [26] Lin Yang and Huey W. Huang. *Science*, **297**(5588), 1877–1879, 2002.
- [27] Elizabeth J. Bolen and Peter W. Holloway. *Biochemistry*, **29**(41), 9638–9643, 1990.
- [28] Richard D. Chambers, Graham Sandford, and Aneela Shah. *Synthetic Commun.*, **26**(10), 1861–1866, 1996.
- [29] Oliver Berger, Olle Edholm, and Fritz Jähnig. *Biophys. J.*, **72**(5), 2002–2013, 1997.
- [30] Erik Lindahl and Olle Edholm. *J. Chem. Phys.*, **113**(9), 3882–3893, 2000.

- [31] D. Peter Tielemans, Justin L. MacCallum, Walter L. Ash, Christian Kandt, Zhitao Xu, and Luca Monticelli. *J. Phys.:Condens. Matter*, **18**(28), S1221–S1234, 2006.
- [32] Andrey A. Gurtovenko. *J. Chem. Phys.*, **122**(24), 244902+, 2005.
- [33] Brett N. Olsen, Paul H. Schlesinger, and Nathan A. Baker. *J. Am. Chem. Soc.*, **131**(13), 4854–4865, 2009.
- [34] Seokmin Shin, Nancy Collazo, and Stuart A. Rice. *J. Chem. Phys.*, **96**(2), 1352–1366, 1992.
- [35] Arvind Hariharan and Jonathan G. Harris. *J. Chem. Phys.*, **101**(5), 4156–4165, 1994.
- [36] Shengting T. Cui, J. Ilja Siepmann, Hank D. Cochran, and Peter T. Cummings. *Fluid Phase Equilibr.*, **146**(1-2), 51–61, 1998.
- [37] William L. Jorgensen, David S. Maxwell, and Julian Tirado-Rives. *J. Am. Chem. Soc.*, **118**(45), 11225–11236, 1996.
- [38] Kirk A. Peterson, Detlev Figue, Erich Goll, Hermann Stoll, and Michael Dolg. *J. Chem. Phys.*, **119**(21), 11113–11123, 2003.
- [39] Jean-Paul Ryckaert and André Bellemans. *Faraday Discuss. Chem. S.*, **66**, 95–106, 1978.
- [40] Brent H. Besler, Kenneth M. Merz, and Peter A. Kollman. *J. Comput. Chem.*, **11**(4), 431–439, 1990.
- [41] Gaëlle Henneré, Patrice Prognon, Françoise Brion, and Ioannis Nicolis. *Chem. Phys. Lipids*, **157**(2), 86–93, 2009.
- [42] R. Jay Mashl, H. Larry Scott, Shankar Subramaniam, and Eric Jakobsson. *Biophys. J.*, **81**(6), 3005–3015, 2001.
- [43] Kalina Hristova, Christopher E. Dempsey, and Stephen H. White. *Biophys. J.*, **80**(2), 801–811, 2001.
- [44] See-Wing Chiu, Mark M. Clark, V. Balaji, Shankar Subramaniam, H. Larry Scott, and Eric Jakobsson. *Biophys. J.*, **69**(4), 1230–1245, 1995.
- [45] H. J. C Berendsen, J. R. Grigera, and T. P. Straatsma. *The Journal of Physical Chemistry*, **91**, 6269–6271, 1987.
- [46] George A. Kaminski, Richard A. Friesner, Julian Tirado-Rives, and William L. Jorgensen. *J. Phys. Chem. B*, **105**(28), 6474–6487, 2001.
- [47] Nilmadhab Chakrabarti, Chris Neale, Jian Payandeh, Emil F. Pai, and Régis Pomès. *Biophys. J.*, **98**(5), 784–792, 2010.

- [48] Berk Hess, Carsten Kutzner, David van der Spoel, and Erik Lindahl. *J. Chem. Theory Comput.*, **4**(3), 435–447, 2008.
- [49] Sun-Joo Lee, Yuhua Song, and Nathan A. Baker. *Biophys. J.*, **94**(9), 3565–3576, 2008.
- [50] Tom Darden, Darrin York, and Lee Pedersen. *J. Chem. Phys.*, **98**(12), 10089–10092, June 1993.
- [51] Michele Parrinello and Aneesur Rahman. *J. Appl. Phys.*, **52**(12), 7182–7190, 1981.
- [52] William G. Hoover. *Phys. Rev. A*, **31**(3), 1695–1697, 1985.
- [53] Berk Hess, Henk Bekker, Herman J. C. Berendsen, and Johannes G. E. M. Fraaije. *J. Comput. Chem.*, **18**(12), 1463–1472, 1997.
- [54] Alan Grossfield and Daniel M. Zuckerman. *Annu. Rep. Comput. Chem.*, **5**, 23–48, 2009.
- [55] Norbert Kučerka, Stephanie Tristram-Nagle, and John Nagle. *J. Memb. Biol.*, **208**(3), 193–202, 2006.
- [56] Balázs Jójárt and Tamás A. Martinek. *J. Comput. Chem.*, **28**(12), 2051–2058, 2007.
- [57] Frederic Gerber, Marie P. Krafft, Thierry F. Vandamme, Michel Goldmann, and Philippe Fontaine. *Biophys. J.*, **90**(9), 3184–3192, 2006.
- [58] Michael Patra, Emppu Salonen, Emma Terama, Ilpo Vattulainen, Roland Faller, Bryan W. Lee, Juha Holopainen, and Mikko Karttunen. *Biophys. J.*, **90**(4), 1121–1135, 2006.
- [59] Andrey A. Gurtovenko and Ilpo Vattulainen. *J. Chem. Phys.*, **130**(21), 215107+, 2009.
- [60] Jonathan N. Sachs, Paul S. Crozier, and Thomas B. Woolf. *J. Chem. Phys.*, **121**(22), 10847–10851, 2004.
- [61] Alexey S. Ladokhin and Peter W. Holloway. *Biophys. J.*, **69**(2), 506–517, 1995.
- [62] Weiping Song, Peter J. Rossky, and Mark Maroncelli. *J. Chem. Phys.*, **119**(17), 9145–9162, 2003.
- [63] Svetlana Baoukina, Luca Monticelli, H. Jelger Risselada, Siewert J. Marrink, and D. Peter Tieleman. *Proceedings of the National Academy of Sciences*, **105**(31), 10803–10808, 2008.
- [64] Cameron Laing, Svetlana Baoukina, and D. Peter Tieleman. *Phys. Chem. Chem. Phys.*, **11**(12), 1916–1922, 2009.
- [65] Hiroki Yokoyama, Hiromichi Nakahara, Takahiro Nakagawa, Satoshi Shimono, Kunihiko Sueishi, and Osamu Shibata. *J. Colloid Interf. Sci.*, **337**(1), 191–200, 2009.
- [66] Jean G. Riess. *Chem. Rev.*, **101**(9), 2797–2920, 2001.

- [67] Tobias Gregor, Gert Schmalisch, Wolfram Burkhardt, Hans Proquitté, Roland R. Wauer, and Mario Rüdiger. *Intens. Care Med.*, **29**(8), 1354–1360, 2003.
- [68] Nicholas S. Faithfull and Jeffry G. Weers. *US Patent 5655521*, August 1997.

6 Tables

6.1 Table 1

Table 1: Force field parameters for PFOB. The bond stretching and angle bending parameters were borrowed from the OPLS-AA force field (37). The energy profiles along the torsional angle were calculated from model molecules: BrCF₂-CF₂CF₃^a and CF₃CF₂-CF₂CF₃^b.

Bond Stretching Parameters								
bond	k_b (kJ mol ⁻¹ nm ⁻²)		r_0 (nm)					
Br-PC	205016.0		0.19450					
PC-PC	224262.4		0.15290					
PC-PEC	224262.4		0.15290					
Angle Bending Parameters								
angle	k_0 (kJ mol ⁻¹ rad ⁻²)		θ_0 (deg)					
Br-PC-PC	577.392		110.0					
PC-PC-PC	488.273		112.7					
PC-PC-PEC	488.273		112.7					
Coefficients of the Torsional Potential Energy Function (kJ mol ⁻¹)								
dihedral angle	C ₀	C ₁	C ₂	C ₃	C ₄			
Br-PC-PC-PC ^a	-21.5787	22.5726	0.9644	-29.3050	2.8832			
PC-PC-PC-PC ^b	-22.1519	2.6823	-7.1261	12.2544	14.8433			
PC-PC-PC-PEC ^b	-22.1519	2.6823	-7.1261	12.2544	14.8433			
Lennard-Jones Parameters for Non-Bonded Interactions								
atom type	σ (nm)		ϵ (kJ mol ⁻¹)					
PC	0.4824		0.3367					
PEC	0.4824		0.4789					
Partial Charges for Long-Range Coulomb Interactions								
atom name	charge (q)							
Br1	0.065							
PC2	-0.205							
PC3	0.03							
PC4	0.03							
PC5	0.03							
PC6	0.03							
PC7	0.03							
PC8	0.02							
PEC9	-0.03							

6.2 Table 2

Table 2: Bulk properties of liquid PFOB. The references for each experimental bulk properties are Riess et al.(66) and Andre et al. (17) for density (ρ), Riess et al. (66), Gregor et al. (67), Faithful et al. (68) for heat of vaporization ($\Delta_{vap}H$), Song et al. (62) for solvation free energy of CF_4 in liquid *n*-hexane (ΔG).

Properties	Experiment	Simulation
ρ (kg L ⁻¹)	1.925 (\pm 0.007)	1.891 (\pm 0.001)
$\Delta_{vap}H$ (kJ mol ⁻¹)	42.67 (\pm 1.276)	41.05 (\pm 0.26)
ΔG (kJ mol ⁻¹)	2.056	2.00 (\pm 0.02)

7 Figure Legends

Figure 1: The structure of a PFOB-NEP interface and its constituent molecules. A) Schematic diagram of a PFOB-NEP interface. PFOB droplet in water is shown as a green sphere. The emulsifying phospholipid monolayer is shown in blue (sphere for head group and lines for lipid tails). B) The structures of constituting molecules. The structure of PFOB is shown with all atoms (green: Br, cyan: carbon, white: fluorine) on the left and with united atoms on the right (large green: Br, small green: perfluorocarbons CF_2 , CF_3). The length of the molecule in its fully extended conformation is 1.02 nm, and the molecular vector is shown with a black arrow. 1-palmitoyl-2-oleyl-phosphatidylcholine lipid is shown with united atoms at the bottom (cyan: hydrocarbon, red: oxygen, blue: nitrogen, gold: phosphorus). The P-N vector is designated by a black arrow.

Figure 2: Two snapshots of the modeled planar PFOB-NEP interface. The top figure shows the starting structure at time 0 ns, and the bottom one shows the structure at time 150 ns in equilibrium. The zoomed in figures on the right show the intercalation of PFOB into the emulsifying monolayers over time. The POPC monolayers with the head groups oriented toward water regions and with lipid tails oriented toward PFOB region are shown in blue. Water is shown in red and white and PFOB is shown in green.

Figure 3: The number densities of each component of the system along the z axis are shown for whole system (solid), POPC monolayer (dashed), water (dotted dash), and PFOB (dotted). The shaded regions in gray mark the density overlap between POPC lipids and PFOB.

Figure 4: Phase separation of PFOB in water in the presence of an emulsifying POPC monolayer. The mass densities of PFOB (green) and water (red) near the interface are shown. The vertical dotted lines show the δ of PFOB interface (δ_{PFOB}), and the vertical dashed lines show that of water interface (δ_{SPC}). The thickness of the δ region was 1.75 nm for PFOB interface and 1.23 nm for water interface, and no overlap is observed.

Figure 5: The change in monolayer thickness examined by the number densities of moieties of POPC lipid. The number densities of control POPC bilayer are plotted with dashed lines, and those of PFOB-NEP interface with solid lines along the z-axis with the same color codes as shown in the figure. To ease the comparison, two profiles are aligned with their maximum densities to be at the zero point on the z-axis. The whole POPC monolayer is shown in black, and lipid moieties in gray colors as shown in the figure.

Figure 6: Changes in system area. A) The distributions of the cross-sectional area of the total monolayer are plotted for control POPC bilayer (black) and PFOB-NEP interface (gray). B) The probe-accessible surface area (ASA) of control POPC bilayer (dark gray) and PFOB-NEP interface (light gray) are plotted. The contributions from hydrophilic and hydrophobic parts of each system are plotted separately. The top insert shows the contribution of each united atom of PFOB starting from Br terminus to CF_3 to the hydrophobic probe-ASA of PFOB-NEP interface. The bottom insert shows the contribution of each component to hydrophobic probe ASA. The left bar shows the sole contribution of POPC (dark gray) in control POPC, and the right bar shows that the contribution of both POPC (light gray) and PFOB (silver) in PFOB-NEP interface.

Figure 7: The order parameters of lipid tails. A) Tail orders of the sn-1 saturated palmitoyl chains are plotted for control POPC bilayer (black) and PFOB-NEP interface (gray). The means are connected by solid lines with one standard error deviations by dotted lines. B) Tail orders of the sn-2 unsaturated oleoyl chains are plotted with the same line types and color codes.

Figure 8: The P-N vector orientation. The mean and one standard error deviation of the P-N vector orientation to the monolayer normal are shown for control POPC bilayer and PFOB-NEP interface.

Figure 9: The structures of PFOB within PFOB-NEP interface. A) The mean molecular end-to-end length of PFOB in each slab of 0.2 nm thickness along the z-axis was calculated. A horizontal dotted line in gray shows the mean length of PFOB in bulk. B) The mean $\cos \theta$, where the θ is an angle between z-axis and the molecular axis of each PFOB molecule, was calculated along the z-axis. The molecular axis was a vector starting from the Br atom to the terminal CF_3 . C) The polarization density of the PFOB weak dipole is plotted along the z-axis. Dashed-gray boxes mark the locations of the two POPC monolayers. The mean is plotted by a solid line and the one standard error deviations are by dashed lines.

Figure 10: Charge densities and electrostatic potentials. To ease the comparison, a half of the system along the z-axis is plotted. A) The charge densities of whole system and individual components are plotted for control POPC (top) and for PFOB-NEP interface (middle). The charge density of PFOB of the PFOB-NEP interface is plotted separately (bottom) to be noticeable. The charge density of the whole system is shown in a solid black line, POPC lipids in a dashed black line, water in a dotted black line, and PFOB in a solid gray line. B) Electrostatic membrane potentials are plotted. The potential of the whole system of control POPC bilayer is plotted on the left panel. The potential of the whole system (black solid) of the PFOB-NEP interface is shown on the right panel. The potential due to PFOB was plotted separately in solid gray line, and the potential generated by POPC monolayer and water is shown in dashed black line.

Figure 11: Structure of melittin bound to the POPC monolayers of the PFOB-NEP interface. A) Two melittin peptides, one in each POPC monolayer, are shown. B) A melittin peptide in the bottom POPC monolayer is shown in detail. Melittin peptides are drawn by a ribbon diagram; the parts in α -helix conformations are shown in magenta, 3-10 helix in blue, turn in green, coil in white. Trp residues are shown in yellow sticks. POPC lipids are drawn with blue lines for tails and with gray and blue balls for head group atoms. Br atom of PFOB is shown in a green ball with perfluorinated chain part in a green stick. Water is shown as white (hydrogen) and red (oxygen) sticks. C) The radial distributions of Br atoms about Trp side chain of melittin in the top (black) and bottom (red) leaflet are plotted as a function distance between the tryptophan side chain and Br atoms.

8 Figures

Figure 1A

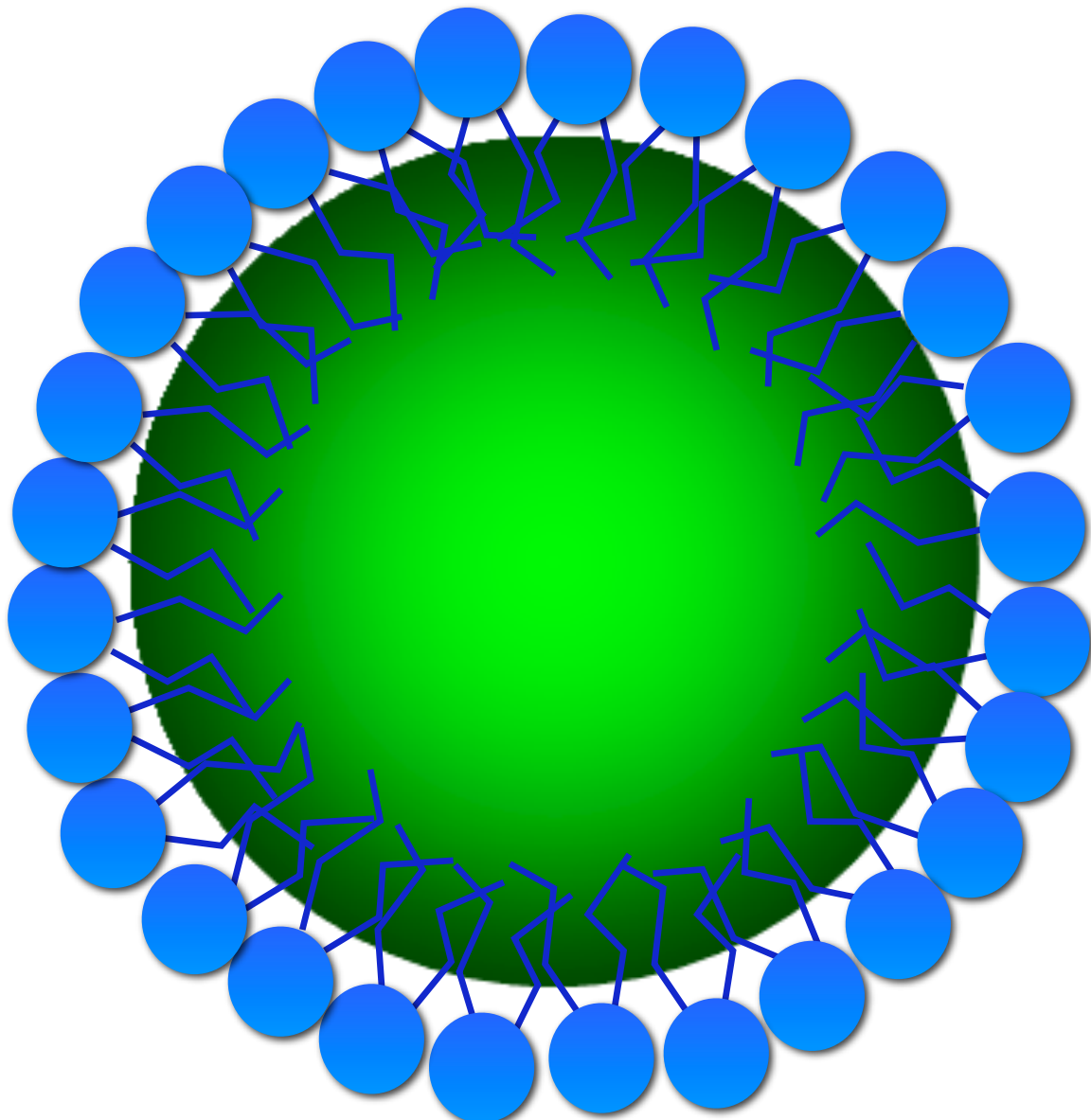


Figure 1B

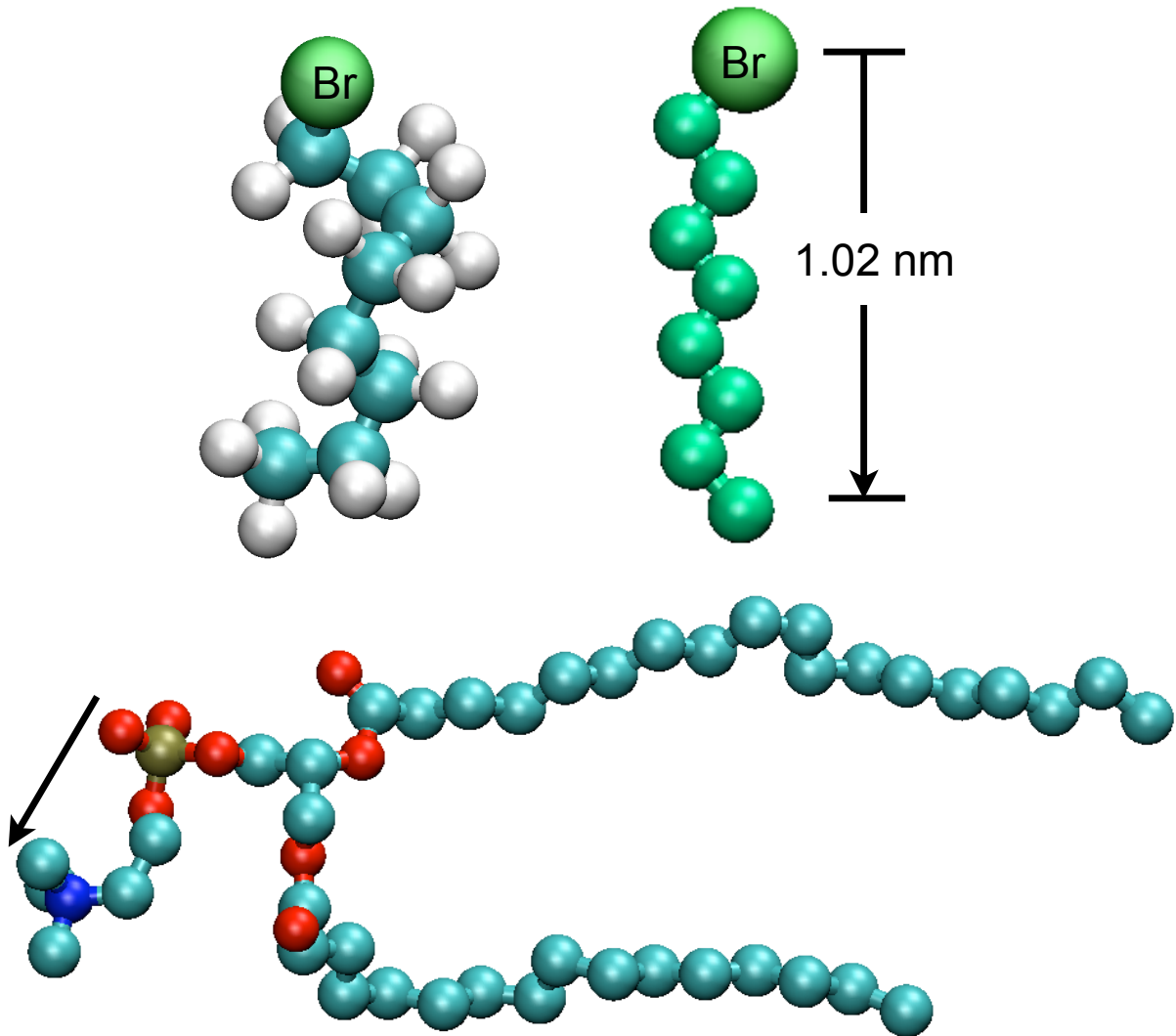


Figure 2

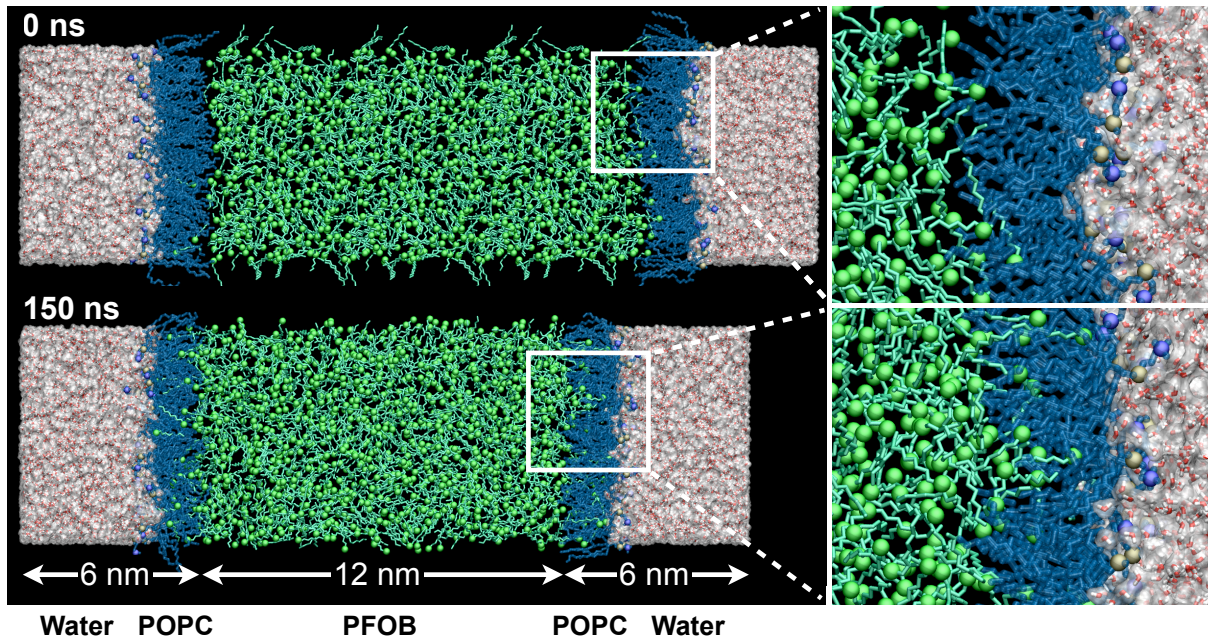


Figure 3

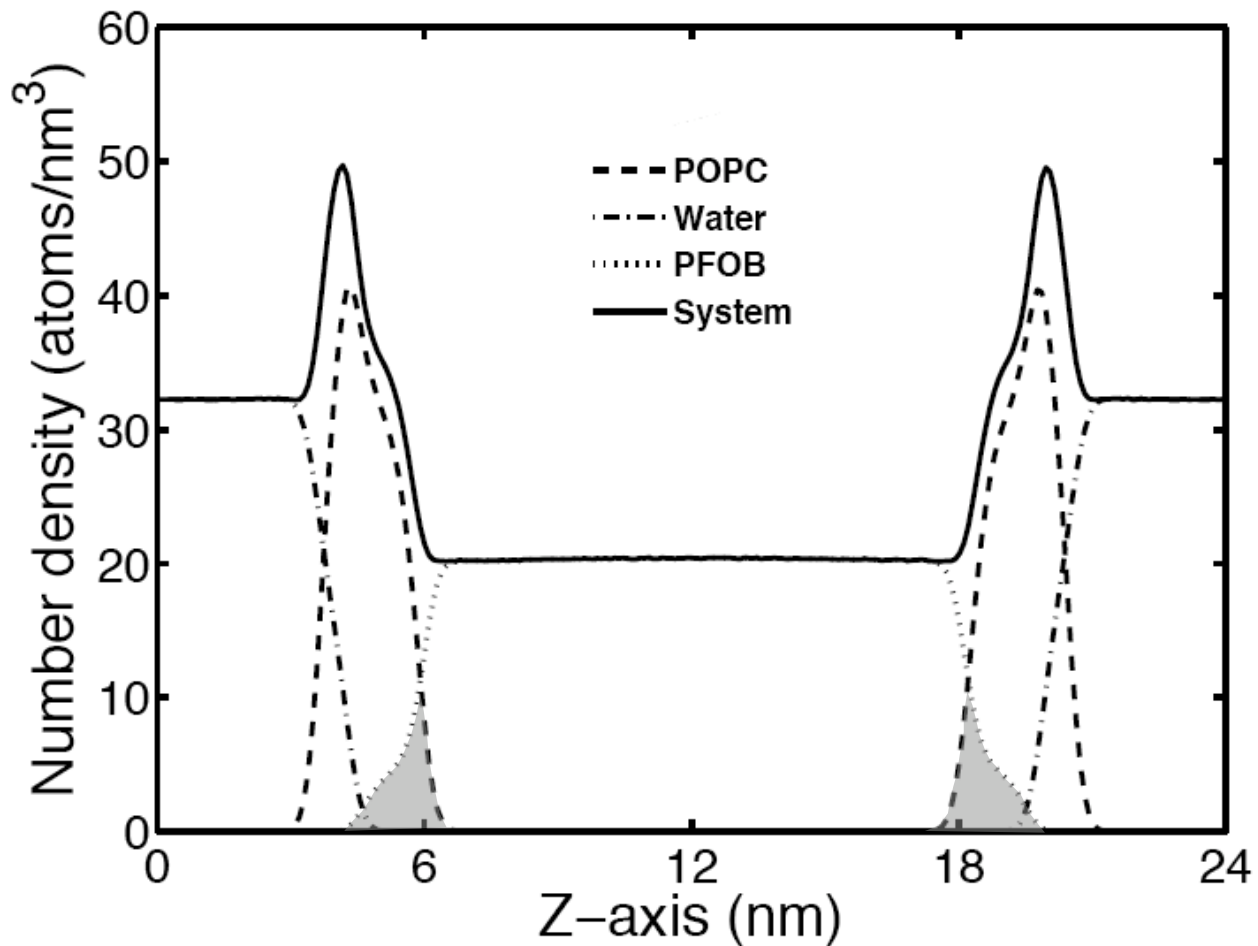


Figure 4

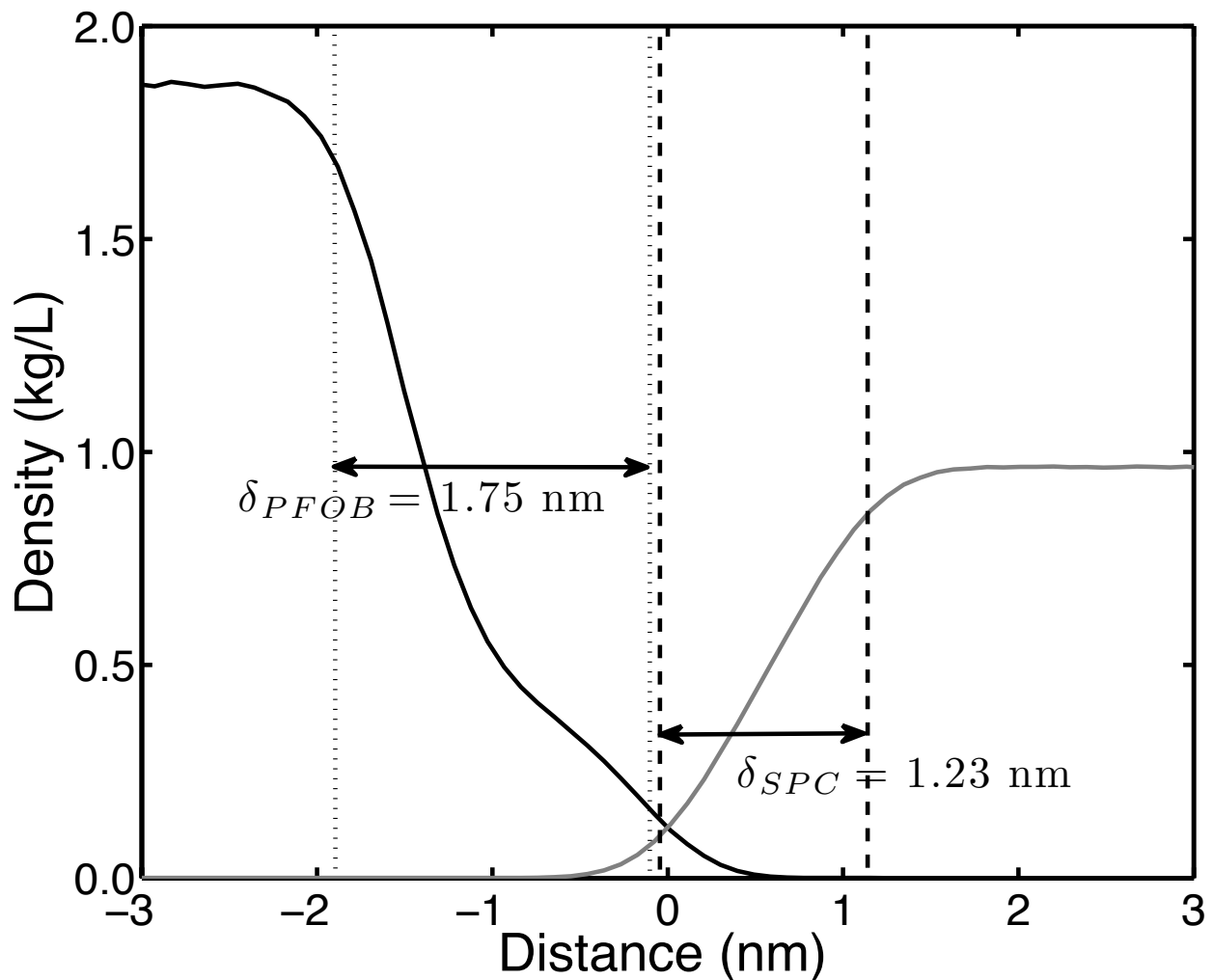


Figure 5

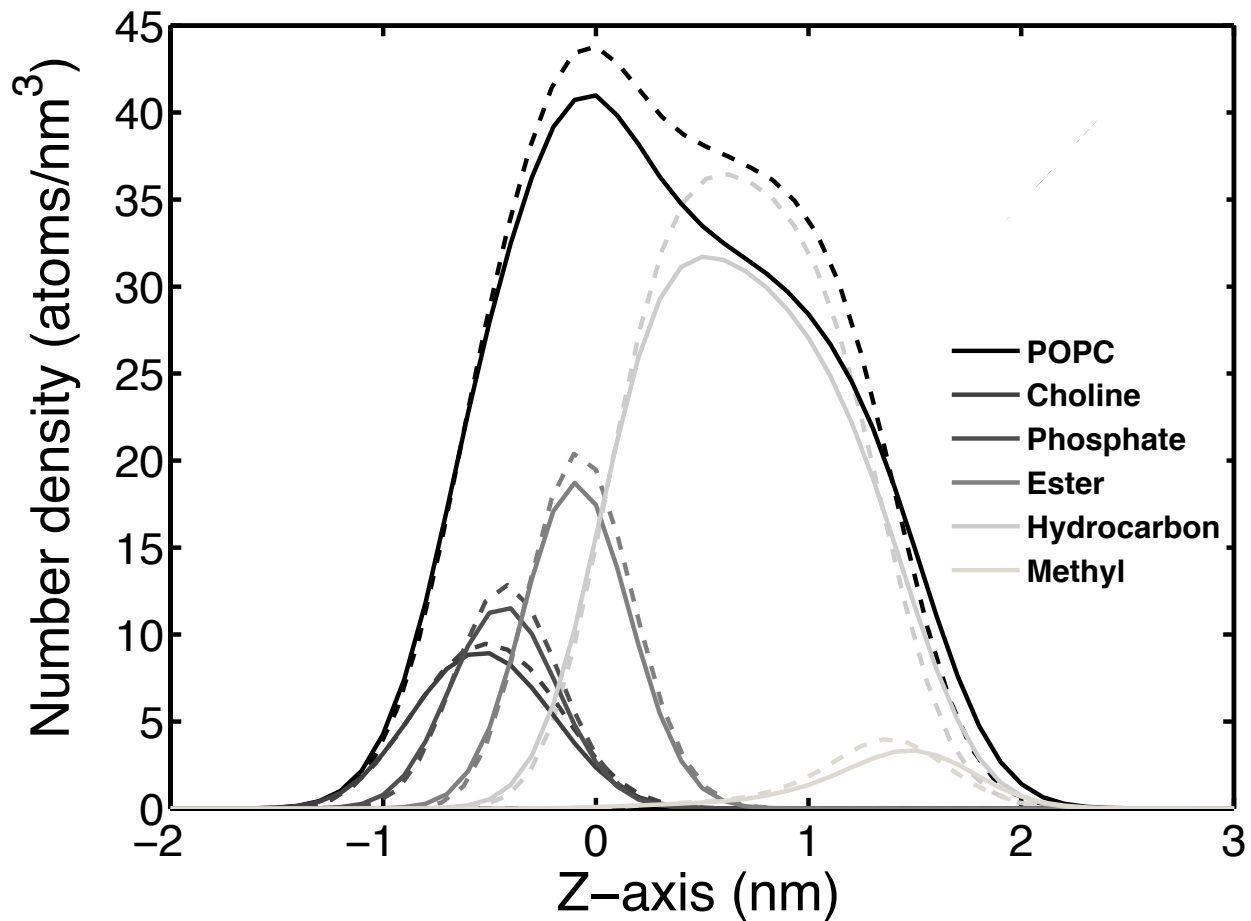


Figure 6A

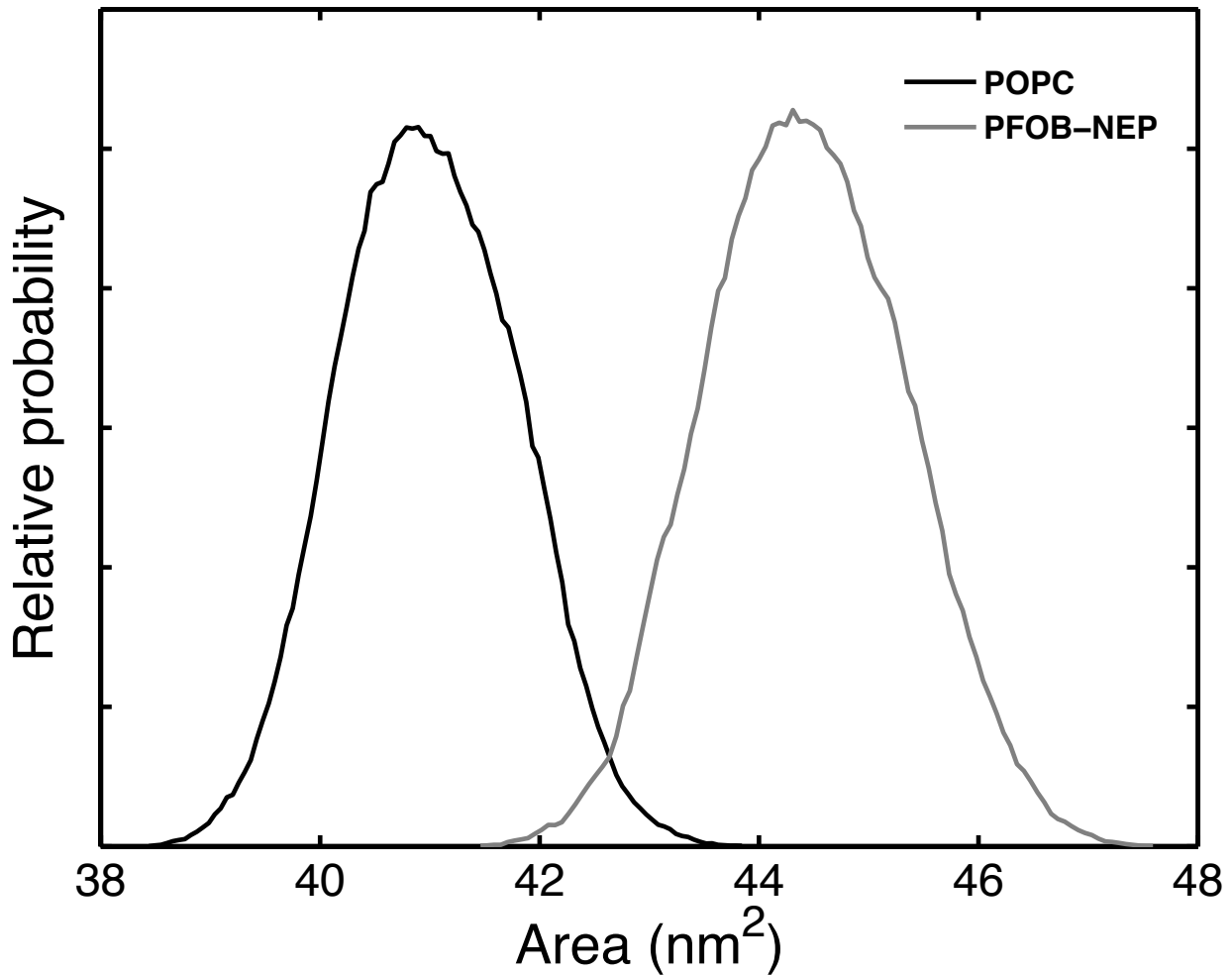


Figure 6B

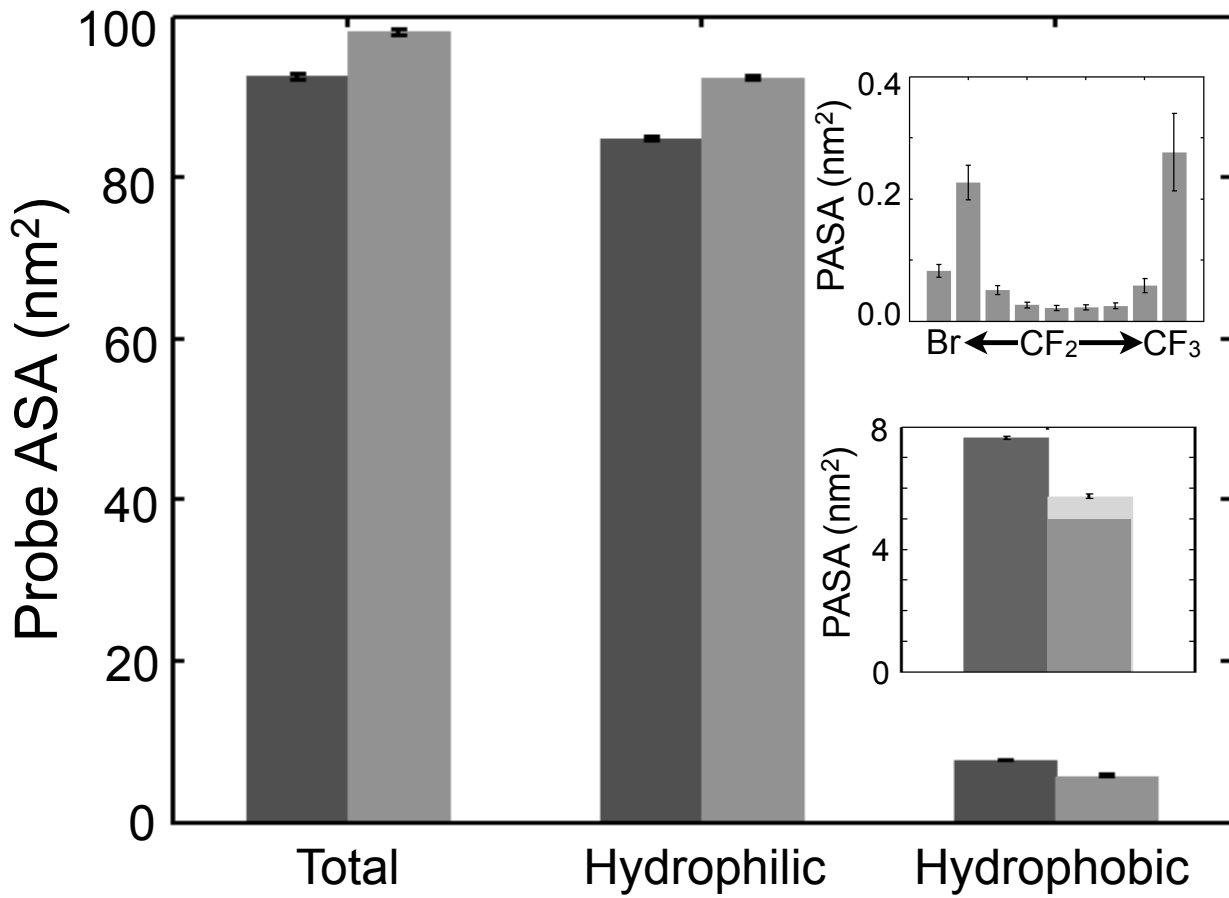


Figure 7A

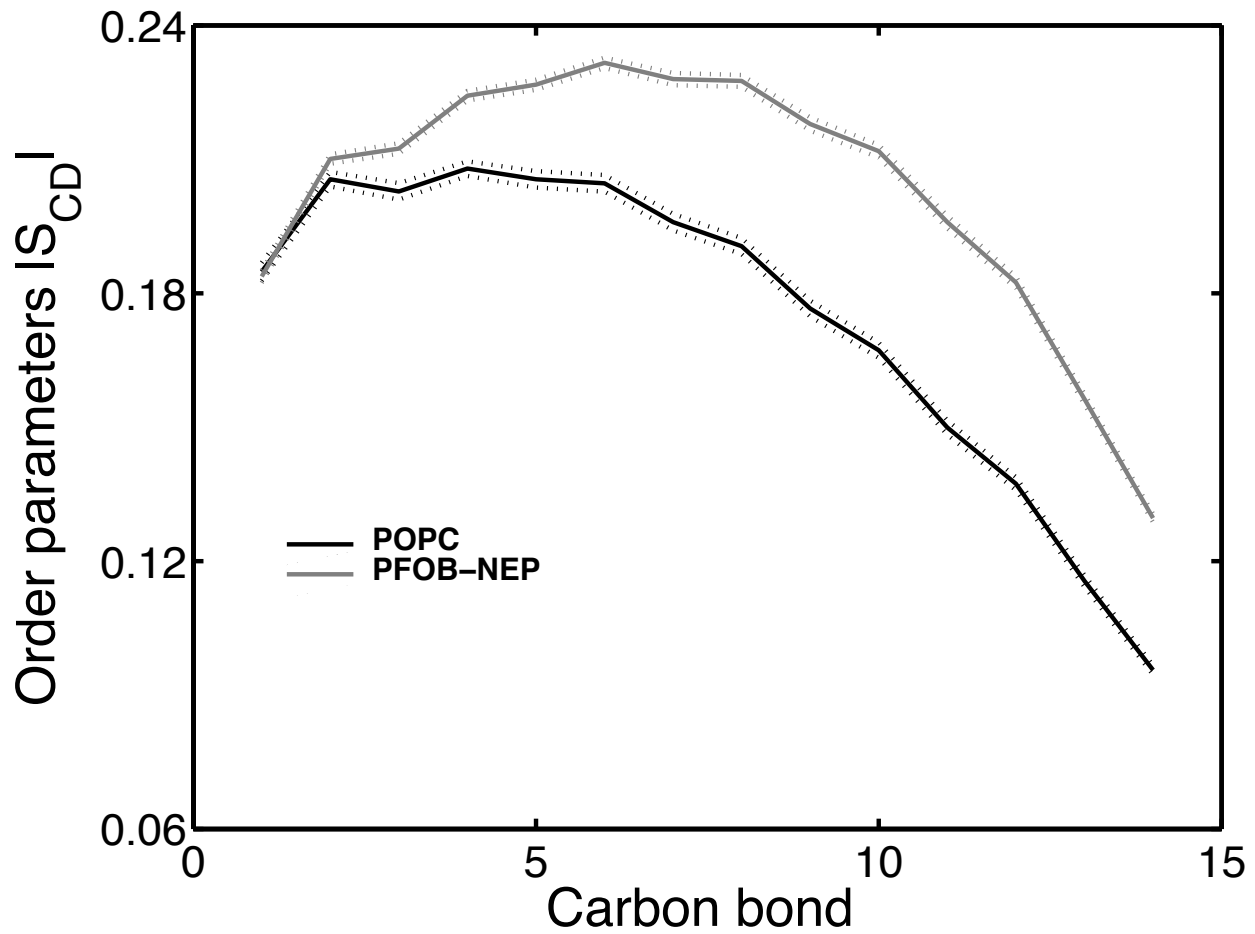


Figure 7B

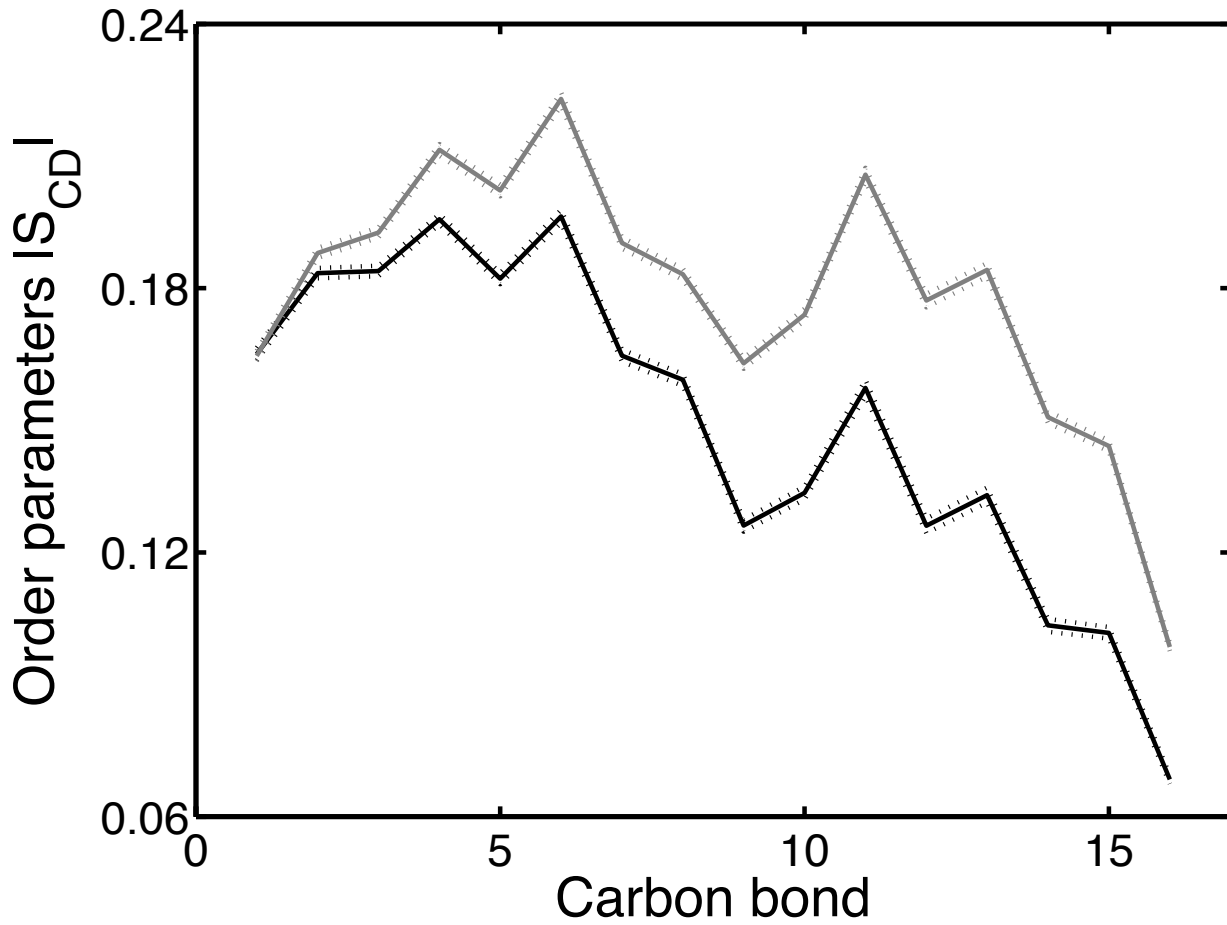


Figure 8

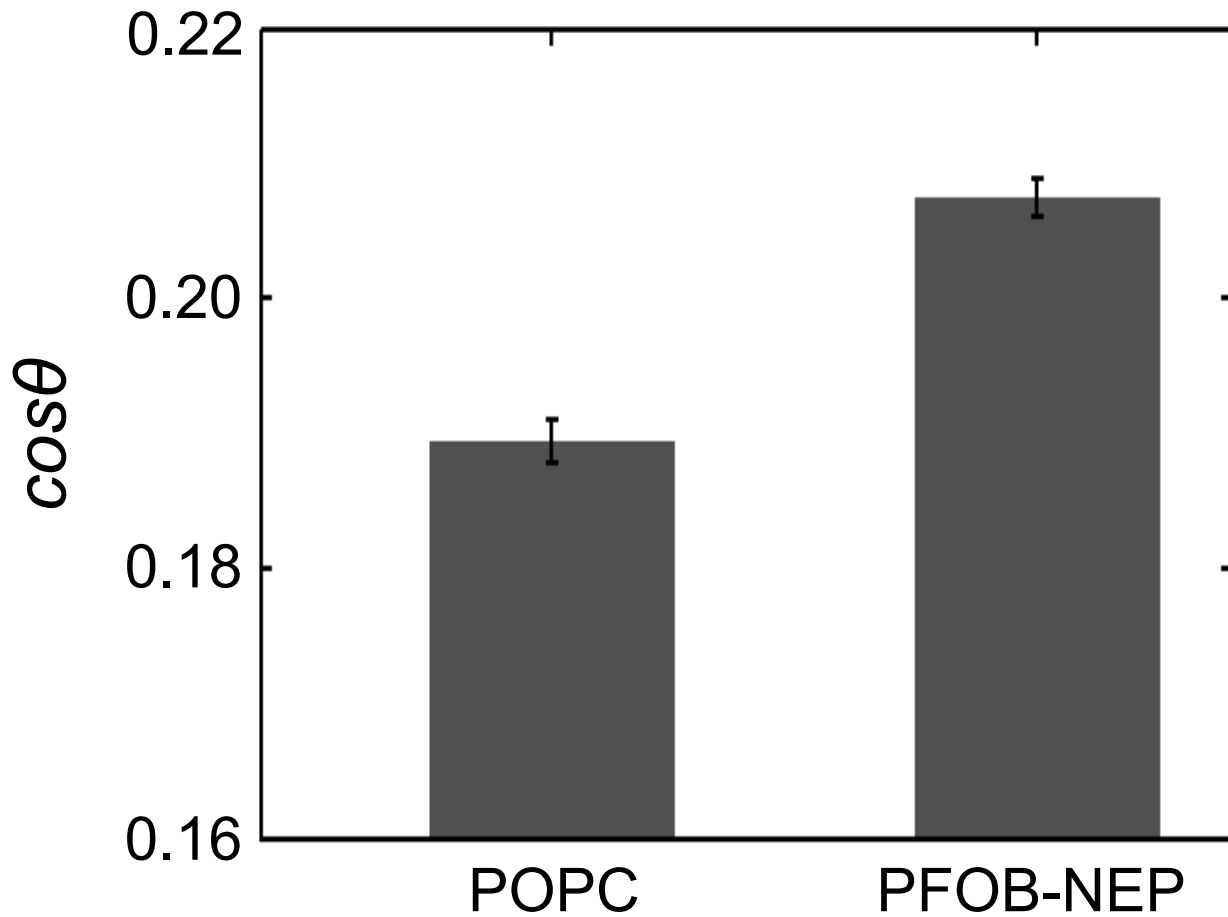


Figure 9A

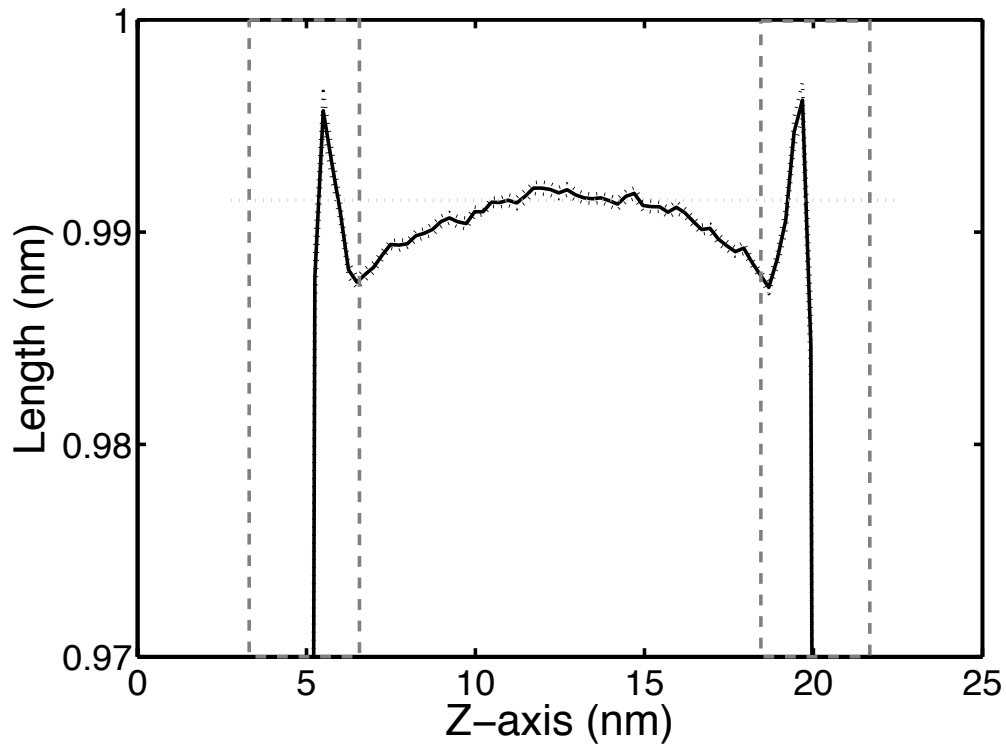


Figure 9B

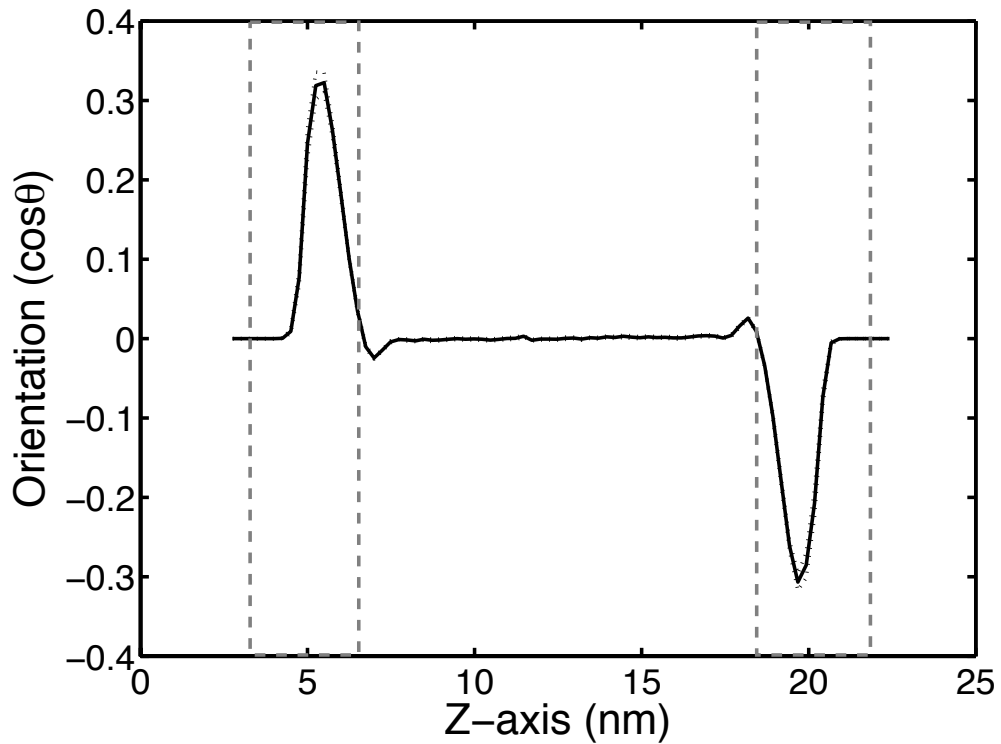


Figure 9C

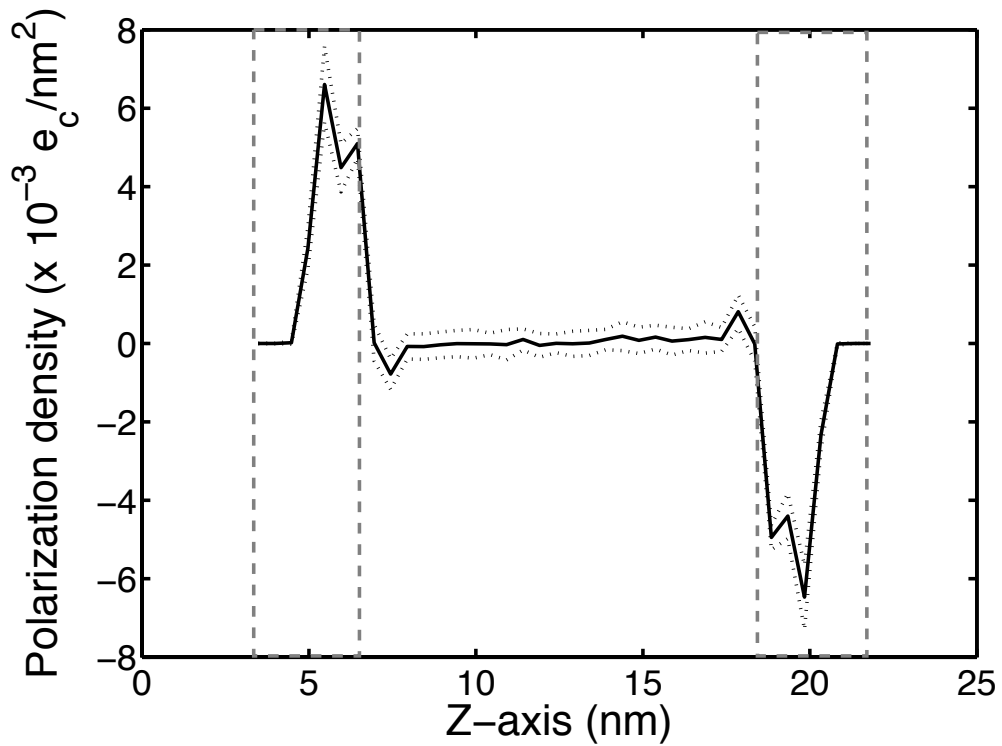


Figure 10A

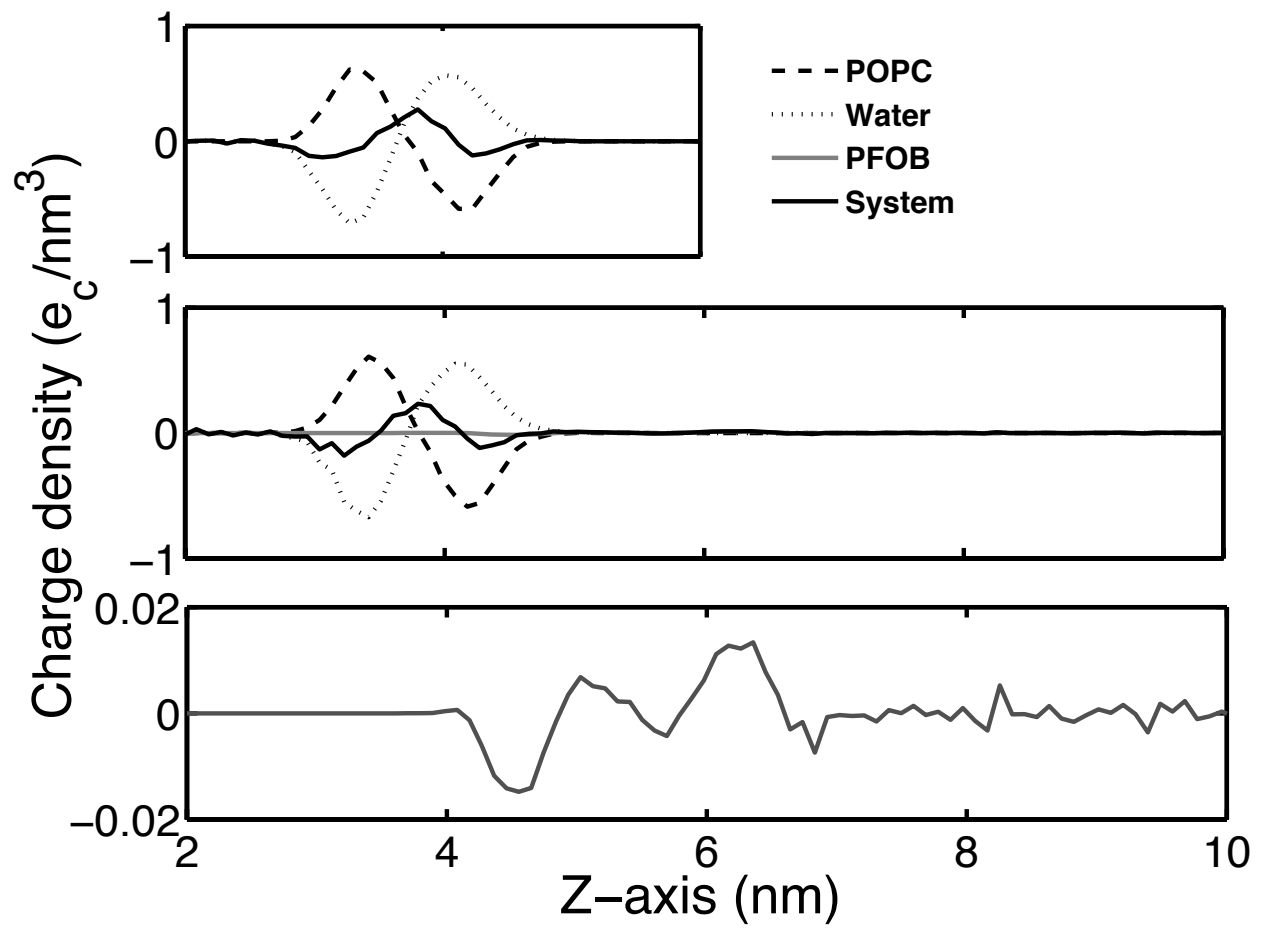


Figure 10B

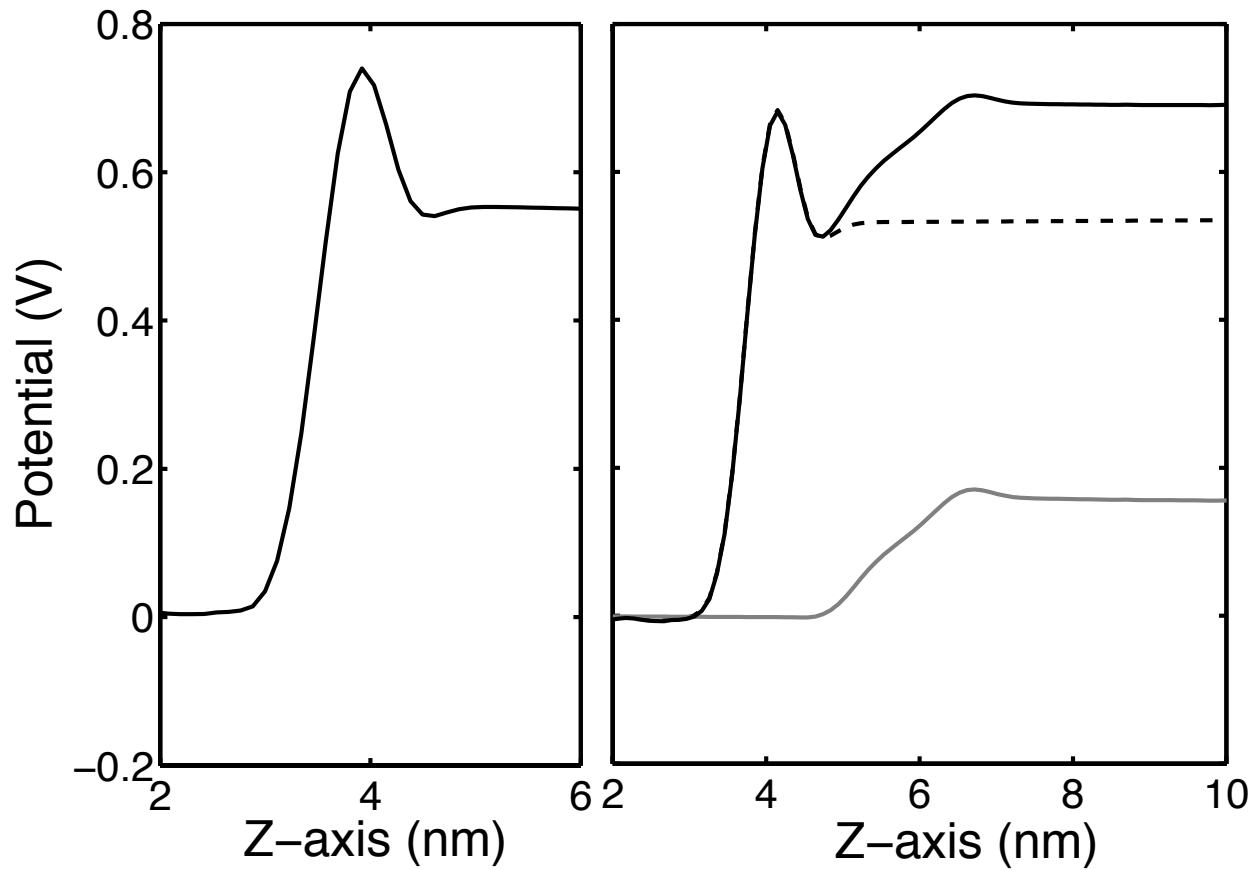


Figure 11

